Hindcasting magma reservoir stability preceding the 2008 eruption of Okmok, Alaska

J. A. Albright[1], P. M. Gregg[1], Z. Lu[2], and J. T. Freymueller[3]

[1]Department of Geology, University of Illinois at Urbana-Champaign, IL, USA.

[2]Huffington Department of Earth Sciences, Southern Methodist University, Dallas, TX, USA.

[3]Department of Earth and Environmental Sciences, Michigan State University, Lansing, MI, USA.

Corresponding author: John Albright (johnaa2@illinois.edu)

Key Points:

- Statistical data assimilation is used to retroactively forecast the 2008 eruption of Okmok volcano, Alaska, which lacked clear precursors.
- Numerical models track the evolving stress state of the Okmok magma system and forecast eruption likelihood at each time step.
- Model forecasts indicate that the system was trending towards tensile failure in the weeks leading up to the 2008 eruption.

Abstract

Volcanic eruptions pose a significant and sometimes unpredictable hazard, especially at systems that display little to no precursory signals. For example, the 2008 eruption of Okmok volcano in Alaska notably lacked observable short-term precursors despite years of low-level unrest. This unpredictability highlights that direct monitoring alone is not always enough to reliably forecast eruptions. In this study, we use the Ensemble Kalman Filter (EnKF) to produce a successful hindcast of the Okmok magma system in the lead up to its 2008 eruption. By assimilating geodetic observations of ground deformation, finite element models track the evolving stress state of the magma system and evaluate its stability using mechanical failure criteria. The hindcast successfully indicates an increased eruption likelihood due to tensile failure weeks in advance of the 2008 eruption. The effectiveness of this hindcast illustrates that EnKF-based forecasting methods may provide critical information on eruption probability in systems lacking obvious precursors.

Plain Language Summary

Volcano monitoring agencies routinely use increases in volcanic unrest as indicators of the potential for eruption. However, for some eruptions, such as the 2008 eruption of Okmok volcano in Alaska, these behaviors can be subtle or missing altogether. In this study, a new statistics-based volcano forecasting approach is used to test whether computer models are able to capture an increase in eruption likelihood leading up to the 2008 event. The models indicate that Okmok was trending towards eruption weeks in advance due to the increased probability of failure of the magma chamber. This successful test indicates that stress around the magma chamber is a strong predictor of volcano stability and that this method could apply to active volcanic systems and improve hazard mitigation efforts.

1 Introduction

The ability to forecast volcanic eruptions has long been a goal for monitoring agencies and the broader scientific community, with the potential to be a powerful tool in mitigating the risks posed by restless volcanoes to human life, property, and activity. Ground deformation in response to magmatic processes has been the focus of much research in this regard (Segall, 2013; Sparks, 2003; Voight et al., 1998), and played a critical role in informing the successful forecast of Axial Seamount's 2015 eruption (Nooner & Chadwick, 2016). Although more general studies of subaerial volcanoes have found a broad correlation between deformation and the timing of eruptions, their relationship is more complex than at Axial Seamount and provides no clear criteria for eruption based on the magnitude or rate of deformation alone (Biggs et al., 2014; Biggs & Pritchard, 2017). In this study, we seek to further explore this relationship by focusing on the mechanical stress state around the magma reservoir, which is both reflected in the surface deformation and ultimately determines when and how the host rock fractures, opening conduits for magma ascent and eruption.

The Ensemble Kalman Filter (EnKF) is a statistical data assimilation technique (Evensen, 1994, 2003, 2009a, 2009b) that improves on earlier formulations of the Kalman filter, many of which have already been successfully applied to geodetic data (Aoki et al., 1999; Fournier et al., 2009; McGuire & Segall, 2003; Miyazaki et al., 2004; Segall & Matthews, 1997). Previous studies in other fields of earth science have demonstrated the EnKF's ability to combine large and/or varied datasets with sophisticated models of nonlinear processes (Allen et al., 2003;

Brusdal et al., 2003; Natvik & Evensen, 2003; Seiler et al., 2009; Wilson et al., 2014), making it particularly well suited for studying active, monitored volcanoes. Following a framework developed by previous studies (Bato et al., 2017; Gregg & Pettijohn, 2016; Zhan & Gregg, 2017), the EnKF is applied to the 2008 eruption of Okmok volcano, Alaska, to produce a retroactive forecast, or "hindcast", of magma system stability. The resulting investigation highlights the importance of tracking volcano stress evolution to forecast eruption potential at active systems.

2 The 2008 eruption of Okmok volcano, Alaska

Although Okmok has hosted large explosive eruptions in the past, including a caldera-forming event at ~2.4 ka (Miller & Smith, 1987), recorded eruptions since 1945 have been dominated by effusive flows emanating from Cone A on the western side of the caldera, with only modest ash columns present (Beget et al., 2005). After its 1997 eruption, Okmok became the target of multiple research efforts including SAR satellite analyses, yearly GPS campaigns (2000-2005), and the installation of 12 permanent seismometers and 4 continuous GPS stations in 2003 (Fig. 1). Continuous inflation was observed starting from the first post-eruption observations in 1997, with episodic pulses of more rapid inflation in the late 1990's, 2002-2003, and 2004-2005, each lasting several months (Fournier et al., 2009; Lu et al., 2010). Geodetic data captured deformation commencing again in early 2008, after 3 years of quiescence and/or slight deflation (Lu et al., 2010). After the failure of the two GPS sites within the caldera in March 2008, InSAR data continued to show inflation until the sudden onset of eruption on July 12 (Fig. 2).

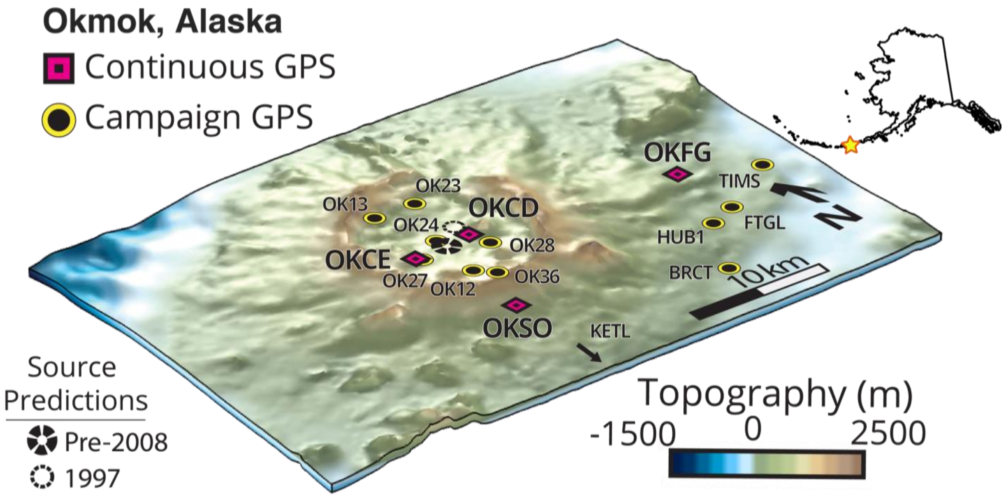

Figure 1. 3D perspective map of Okmok Volcano, Alaska, showing topography and locations of GPS stations used in this study. Black markers compare the center of pre-eruptive inflation calculated in this study with the coeruptive deflation center found for the 1997 eruption (Mann et al., 2002). Cone A lies south of OKCE, while Cone D lies slightly east of station OKCD.

Unlike the 1997 eruption, the 2008 event formed a new vent near Cone D on the eastern side of Okmok caldera (Larsen et al., 2009). Due to phreatomagmatic interactions between fresh magma and the local water table, the explosive eruption reached VEI 4 and produced a 16 km high ash column (Larsen et al., 2009). Despite the magnitude of the eruption, it lacked a clear precursory signal in its ground deformation. Furthermore, seismic activity had been quiet in the preceding months until a 3-5 hour long, low-magnitude precursory earthquake swarm was recorded 11 hours prior to the 2008 eruption (Larsen et al., 2009).

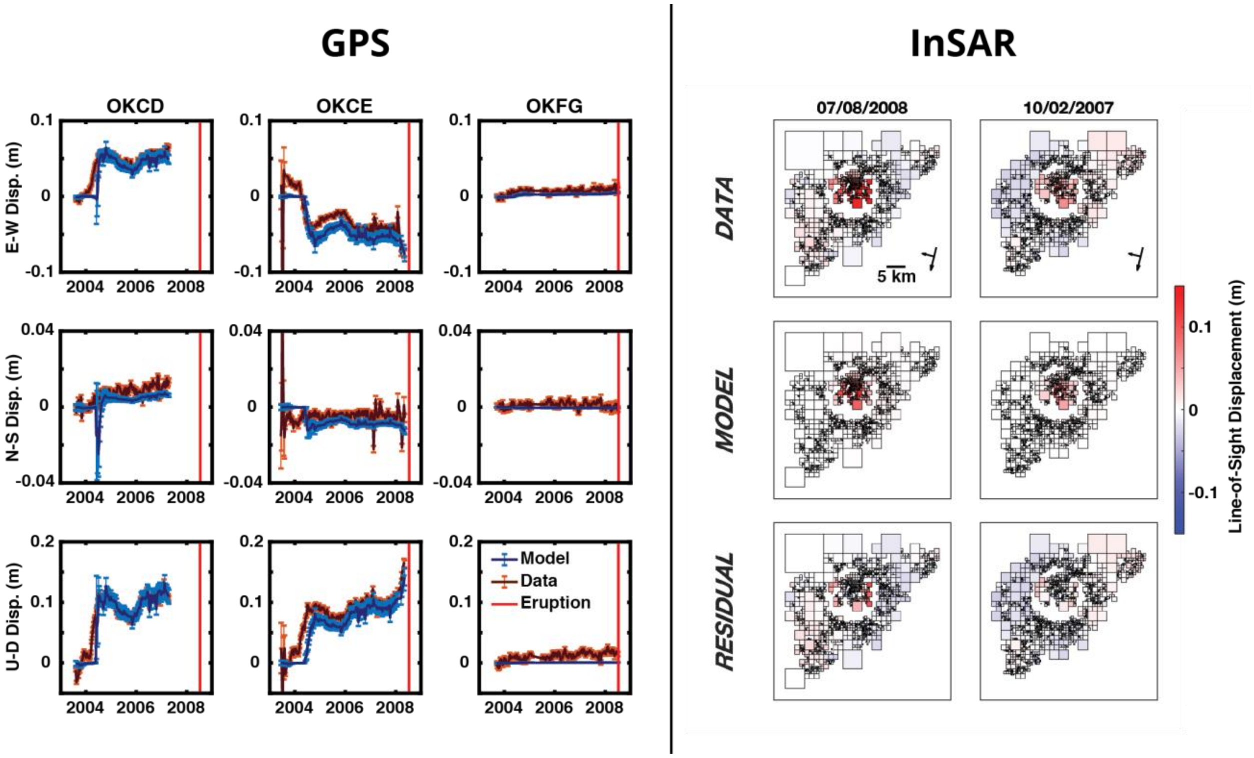

Figure 2. Comparison of deformation predicted by the EnKF assimilation results with original data from selected GPS stations and InSAR images. GPS data have been averaged into 10-day bins, while the cumulative InSAR data have been downsampled via a quadtrees algorithm and averaged within the boxes pictured. The EnKF approach sequentially assimilates both GPS and InSAR data as they become available. Comparisons with all available data and additional model runs with GPS only and InSAR only calculations are available in the Online Supplementary Information.

3 Geodetic data assimilation to provide model forecasts

The EnKF is utilized to combine geodetic observations of surface deformation at Okmok with finite element models (FEM) of the evolving Okmok magma system. Specifically, GPS and InSAR data are assimilated into a two-dimensional, axisymmetric, linear elastic FEM. In this implementation, the EnKF analysis consists of 300 models, which are updated sequentially in parallel as observations become available from GPS and/or InSAR. The EnKF tracks the observed deformation, providing a good fit to the geodetic data (Fig. 2). Although there is slight misfit due to the assumed symmetry of the model, the modeled pressure source is in relative agreement with previous static inversions (Biggs et al., 2010; Fournier et al., 2009; Lu et al., 2005, 2010). Although petrologic and geochemical findings suggest a more complex reservoir geometry, with several distinct shallow reservoirs fed by a deeper source (Larsen et al., 2013), the geodetic data considered here and in previous studies are sufficiently accounted for by a single-source model and lack clearly distinct signals from both a shallow and a deep reservoir.

Overall, a joint GPS+InSAR assimilation approach works best for Okmok. In particular, InSAR provides critical spatial coverage between GPS stations, while continuous GPS signals provide important model updates during temporal gaps in InSAR data collection. Additional EnKF experiments were conducted to investigate the assimilation of GPS or InSAR data alone, and are provided in the Supplementary Information. However, the single-technique assimilation approaches both failed to successfully hindcast the 2008 eruption, indicating that the combination of spatial and temporal data coverage is necessary. In particular, the GPS-only assimilation underestimates the depth of the reservoir relative to the joint assimilation, overestimates its lateral extent and aspect ratio (Fig. S10), thus predicting failure prematurely (Fig. S11). The loss of data from two malfunctioning stations within the caldera most likely contributed to this poor performance as well, since the absence of such proximal stations can significantly reduce the accuracy of the EnKF (Zhan & Gregg, 2017). In contrast to the GPS results, the pressure source modeled by the InSAR-only assimilation overestimates the stability of the reservoir and fails to forecast any eruption-producing failure in 2008 (Fig. S14).

4 The evolving state of Okmok's magma system

An advantage of the EnKF approach is that model parameters are updated at each time step of the assimilation, allowing for the evolution of the magma reservoir to be evaluated (Fig. 3). Additionally, the observed spread of the parameter values within the ensemble provides a first-order estimate of uncertainty in each parameter (Evensen, 2009a). We assimilated data from 2003-2008, starting with the first SAR image of our dataset on June 10, 2003. Uncertainty is high during the first year of the assimilation due to the volcano being in a period of quiescence with little deformation. However, all of the parameters quickly converge in 2004, coinciding with the first observed period of major inflation.

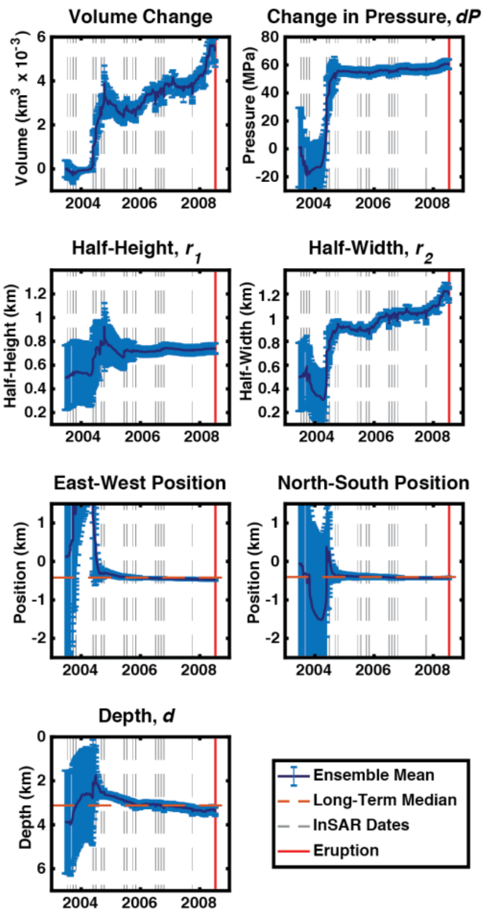

Figure 3. EnKF predictions for the 6 variables modeled in this study, as well as an aggregate volume change term derived from the other values. Uncertainty at each time step is given by twice the observed standard deviation in each parameter across the ensemble (N = 300).

The resultant pressure source location agrees with previous studies, which estimate a stationary source located ~3 km beneath the center of Okmok's caldera (Biggs et al., 2010; Fournier et al., 2009; Lu et al., 2005, 2010). To characterize the magma reservoir, our model assumes an ellipsoidal shape and separately tracks the half-height, half-width, and pressure change, which are then combined into a single volume change term according to the bulk modulus of the host rock. Pressure increases ~60 MPa during the 2004-2005 inflation event, but then remains mostly stable throughout the rest of the assimilation, with only slight increases during the second period of inflation in 2008. Similarly, the reservoir half-height remains somewhat constant through 2008, leaving an increasing half-width as the primary driver of inflation. The model result of lateral reservoir growth, rather than changing pressure, has significant implications for our understanding of the evolution of the magma system in the lead up to the eruption.

Previous studies of GPS deformation at Okmok observed non-zero circumferential motion prior to the eruption (Fournier et al., 2009; Freymueller & Kaufman, 2010). This phenomenon requires changes in the source geometry and cannot be reproduced through increases in pressure alone. The observed shift in the main eruption vent from Cone A to Cone D may also imply a change in the geometry of the magma system more generally, but our models do not make any specific predictions as to how magma reaches the surface once the reservoir has mechanically failed.

5 Linking model forecasts to eruption triggers

At each time step throughout the assimilation, we track three potential catalysts for eruption: overpressure, Mohr-Coulomb failure, and tensile rupture. The excess pressure within the reservoir quickly exceeds 10-40 MPa (often cited as a limit for initiating and propagating a dike to the surface; e.g., Rubin, 1995) by late 2004 and then remained effectively constant leading up to the eruption. These findings suggest that a critical overpressure alone was not sufficient to trigger the 2008 eruption. Within a region surrounding and overlying the magma reservoir we also tested for Mohr-Coulomb failure. Although the majority of models in the ensemble showed some degree of failure throughout the assimilation, the effect was always localized near the surface of the model space and never resembled the through-going failure suggested as an eruption trigger by other studies (Cabaniss et al., 2018; Gregg et al., 2018; Gregg et al., 2012). Finally, we define tensile rupture of the reservoir to occur when the least compressive stress exceeds the rock's tensile strength at some point along the reservoir wall (Grosfils, 2007).

The percentage of ensemble members in tensile failure is used as an aggregate and relative measure of reservoir stability throughout the assimilation (Fig. 4a). Unlike overpressure and Mohr-Coulomb failure, which tend to vary little over the observed time period, the abundance of tensile failure strongly correlates with the behavior of the system, displaying two peaks in 2005 and 2008 during or shortly after the periods of greatest inflation. The tensile strength assumed for the wall rock also plays a significant role in determining the system's stability. When a strength of 0 MPa is assumed, approximating a case in which preexisting fractures have compromised the rock's cohesion, failure is present in ~20% more ensemble members than when a tensile strength of 10 MPa is used. However, regardless of the strength assumed, the entire ensemble trends towards higher tensile stresses and by extension likelihood of failure throughout 2008 (Fig. 4b). This tensile rupture occurs predominantly along the reservoir's outer rim, which lies in close proximity to the eruption vent near Cone D (Fig. 4c). Moreover, the fact that this spike occurs within months of the actual onset of eruption suggests that our assimilation framework is able to reliably account for the accumulation of stress around the magma reservoir through the preceding years, producing a successful hind-cast of the 2008 event. Such information may have allowed AVO to raise the alert level at Okmok and increase monitoring efforts, potentially catching the pre-eruptive seismicity as well as the eruption itself.

An alternative triggering mechanism not directly modeled in this study due to technical limitations is the progressive weakening of the host rock during pre-eruptive deformation. Previous studies at other systems (e.g., Got et al., 2017), have shown that fracturing and seismicity in the edifice above the reservoir can produce a significant weakening in the rock's mechanical properties. However, given the scant and low-intensity nature of the pre-eruptive seismic signal at Okmok (Larsen et al., 2009) and the lack of fault-related deformation in the geodetic data, it is unlikely that enough fracturing occurred in the months before the eruption to significantly impact its onset. Such a lack of fracturing would also agree with our assimilation's prediction of very little Mohr-Coulomb failure.

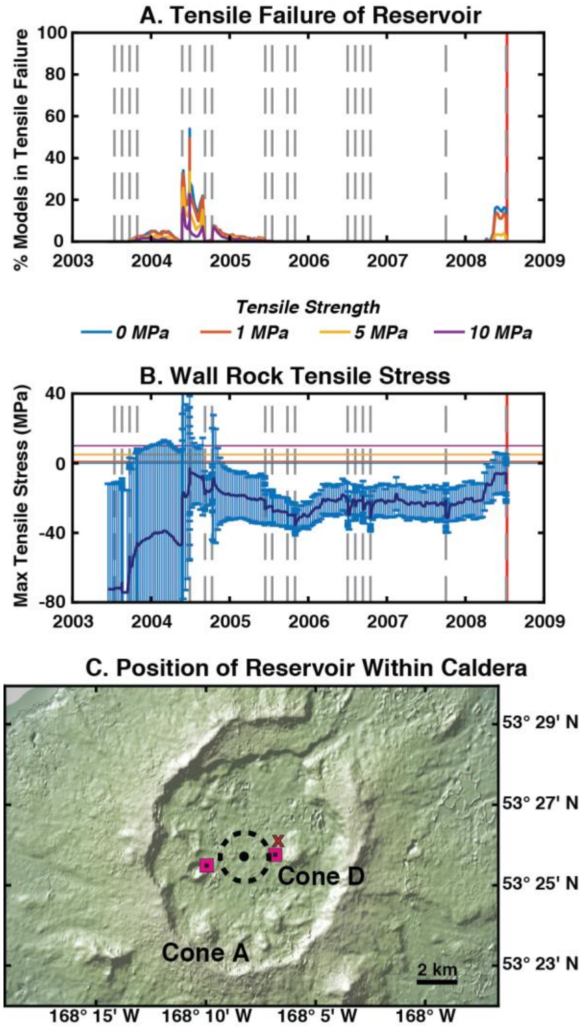

Figure 4. The evolution of predicted tensile failure in the lead up to the 2008 eruption. **A.** Percentage of ensemble members exceeding tensile failure criterion at each time step for 4 different tensile strengths. An ensemble member is considered to be in failure if tensile stress exceeds the given tensile strength at any point along the reservoir wall. **B.** Maximum tensile stress calculated along the reservoir wall by EnKF assimilation at each time step. Solid line indicates ensemble mean with 2σ error bars. Horizontal lines indicate threshold tensile strengths. **C.** Map view of Okmok Caldera showing the center (dot) and extent (dotted line) of the forecasted reservoir (black) relative to nearby continuous GPS stations (purple squares), intra-caldera cones, and the primary vent of the 2008 eruption (red X).

6 Implications for eruption forecasting at volcanic systems

Our results show that the EnKF is a powerful tool for combining multiple streams of observational data with complex numerical models to provide a detailed picture of magma reservoir dynamics at active volcanic systems. Moreover, in successfully reproducing Okmok's 2008 eruption we have also shown the EnKF's potential as a forecasting tool to be used by monitoring agencies. The EnKF technique could theoretically be applied in real time, providing an ongoing, up-to-date model of the magma reservoir and its likelihood of mechanical failure independently of more immediate precursors. Moreover, as a framework the EnKF is very flexible and can easily be adapted for use with different predictive models, as discussed below, and with any dataset that could reasonably be predicted by those models. Although this study only uses GPS and InSAR data, other observations such as ground tilt could have also been used if available. Given the relative novelty of this approach in volcanology, however, there are still many questions to ask and technical limitations to overcome before the application of the EnKF can reach its full potential.

First of all, there is the question of how to distinguish changes in source parameters from artifacts of model convergence. Previous synthetic tests of the EnKF predict that the ensemble converges from its initial wide distribution within the first few time steps, with all subsequent changes in the modeled parameters being due primarily to changes in the source (Gregg & Pettijohn, 2016; Zhan & Gregg, 2017). In this study, however, most parameters do not begin to narrow until nearly a year after the start of the assimilation. Although this effect is most likely due to the low magnitudes of deformation during the initial time steps providing the EnKF little basis on which to distinguish the performance of one ensemble member against another, the question of when the results become meaningful still remains. A sudden increase in the modeled overpressure during 2004, for instance, coincides with both the first major period of inflation and the initial convergence of the parameters. Although the observed deformation may be driven by an increase in pressure as modeled, this case is difficult to distinguish from the possibility that the pressure change is an artifact of convergence and that the deformation was driven by changes in other parameters such as the half-width.

We must next consider the limitations of the numerical models being used within the EnKF framework. As we develop our workflow we have primarily chosen restrictive models (e.g., axisymmetry, elastic rheology) that can easily be compared to and benchmarked against accepted analytical solutions (McTigue, 1987; Mogi, 1958; Yang et al., 1988). Although these simplifications make the assimilation computationally easier, actual volcanic systems host a variety of effects that we currently do not account for, including layered, non-elastic, or temperature-dependent rheology (Del Negro et al., 2009; Gregg et al., 2013; Long & Grosfils, 2009; McTigue, 1987), pore pressure (Albino et al., 2018; Grosfils et al., 2015), overlying features such as faults or edifices (Gregg et al., 2018; Grosfils et al., 2015), and far field stresses (Cabaniss et al., 2018; Martí et al., 2016), all of which may alter when and how the reservoir fails. The EnKF, however, is model-independent and does not need to be reformulated for each application like other forms of Kalman Filters (Evensen, 1994; Grewal & Andrews, 2008; Julier et al., 2000). As our approach is tested and benchmarked, it will be relatively simple to substitute more complex or competing models in order to observe how they may affect the assimilation's outcomes and the resulting conclusions. However, time-dependent models, such as ones that use viscoelasticity or that simulate magma flux directly (Gregg et al., 2018; Le Mével et al., 2016), may be more difficult to incorporate into an EnKF framework. In particular, these formulations pose additional challenges in terms of computational load and in defining the initial conditions. While a time-dependent version of our approach has been tested (Gregg & Pettijohn, 2016), it required running the models from time zero at each time step, which becomes computationally prohibitive.

Although the question of how to define initial conditions is particularly important when using time-dependent models, it should be considered for any implementation of the EnKF. In this study, for instance, the net deformation state of the volcano at the start of our assimilation is not considered due to lack of data. Our models therefore only account for the stresses that built up over the observed period, and any previous stress accumulation may cause tensile and/or Mohr-Coulomb failure to occur sooner than predicted by the assimilation. Ideal targets for future studies would therefore be systems with short recurrence intervals and geodetic observations spanning multiple eruption cycles, such that all observations can be made relative to the end of a previous eruption (e.g., Sierra Negra and Fernandina, Galapagos; Aria/Sakurajima, Japan; Agung and Sinabung, Indonesia). Regardless, the EnKF is a powerful and flexible tool that could potentially be used to improve our understanding of any system with sufficient data.

Acknowledgements

This work was supported by a U.S. National Science Foundation Graduate Research Fellowship (Albright), grants from the U.S. National Science Foundation (NSF CAREER - 1752477, NSF OCE MGG - 1634995, Gregg), U.S. National Aeronautics and Space Administration (80-NSSC19K-0357 Gregg and Lu, and ESI13-0031 Lu and Freymueller). We would like to thank Lei Zhang of Hong Kong Polytechnic University and Jin Woo Kim of Southern Methodist University for the help in acquiring and processing the InSAR data. We are also grateful for helpful discussions with Y. Zhan, C. Pettijohn, H. Cabaniss, R. Goldman, V. Romano, and the UIUC Geodynamics Group. GPS data used in this investigation are available at https://www.unavco.org/data. InSAR data were previously published by Lu et al. (2010). Model data in support of this manuscript are published in the PANGAEA data repository and available online (https://doi.org/10.1594/PANGAEA.904432).

References

Albino, F., Amelung, F., & Gregg, P. (2018). The Role of Pore Fluid Pressure on the Failure of Magma Reservoirs: Insights From Indonesian and Aleutian Arc Volcanoes: THE ROLE OF PORE PRESSURE ON FAILURE. *Journal of Geophysical Research: Solid Earth*, *123*(2), 1328–1349. https://doi.org/10.1002/2017JB014523

Albright, John A; Gregg, Patricia M; Lu, Zhong; Freymueller, Jeffrey T (2019): EnKF Data Assimilation Outputs Modeling Preeruptive Deformation at Okmok AK, 2003-2008. PANGAEA, https://doi.org/10.1594/PANGAEA.904432,

Allen, J. I., Eknes, M., & Evensen, G. (2003). An Ensemble Kalman Filter with a complex marine ecosystem model: hindcasting phytoplankton in the Cretan Sea. *Annales Geophysicae*, *21*(1), 399–411. https://doi.org/10.5194/angeo-21-399-2003

Aoki, Y., Segall, P., Kato, T., Cervelli, P., & Shimada, S. (1999). Imaging Magma Transport During the 1997 Seismic Swarm off the Izu Peninsula, Japan. *Science*, *286*(5441), 927–930. https://doi.org/10.1126/science.286.5441.927

Bato, M. G., Pinel, V., & Yan, Y. (2017). Assimilation of Deformation Data for Eruption Forecasting: Potentiality Assessment Based on Synthetic Cases. *Frontiers in Earth Science*, *5*. https://doi.org/10.3389/feart.2017.00048

Beget, J. E., Larsen, J. F., Neal, C. A., Nye, C. J., & Schaefer, J. R. (2005). *Preliminary volcano-hazard assessment for Okmok Volcano, Umnak Island, Alaska* (No. RI 2004-3). Alaska Division of Geological & Geophysical Surveys. https://doi.org/10.14509/7042

Biggs, J., & Pritchard, M. E. (2017). Global Volcano Monitoring: What Does It Mean When Volcanoes Deform? *Elements*, *13*(1), 17–22. https://doi.org/10.2113/gselements.13.1.17

Biggs, J., Lu, Z., Fournier, T., & Freymueller, J. T. (2010). Magma flux at Okmok Volcano, Alaska, from a joint inversion of continuous GPS, campaign GPS, and interferometric synthetic aperture radar. *Journal of Geophysical Research*, *115*(B12). https://doi.org/10.1029/2010JB007577

Biggs, J., Ebmeier, S. K., Aspinall, W. P., Lu, Z., Pritchard, M. E., Sparks, R. S. J., & Mather, T. A. (2014). Global link between deformation and volcanic eruption quantified by satellite imagery. *Nature Communications*, *5*(1). https://doi.org/10.1038/ncomms4471

Brusdal, K., Brankart, J. M., Halberstadt, G., Evensen, G., Brasseur, P., van Leeuwen, P. J., et al. (2003). A demonstration of ensemble-based assimilation methods with a layered OGCM from the perspective of operational ocean forecasting systems. *Journal of Marine Systems*, *40–41*, 253–289. https://doi.org/10.1016/S0924-7963(03)00021-6

Cabaniss, H. E., Gregg, P. M., & Grosfils, E. B. (2018). The Role of Tectonic Stress in Triggering Large Silicic Caldera Eruptions. *Geophysical Research Letters*, *45*(9), 3889–3895. https://doi.org/10.1029/2018GL077393

Del Negro, C., Currenti, G., & Scandura, D. (2009). Temperature-dependent viscoelastic modeling of ground deformation: Application to Etna volcano during the 1993–1997 inflation period. *Physics of the Earth and Planetary Interiors*, *172*(3–4), 299–309. https://doi.org/10.1016/j.pepi.2008.10.019

Evensen, G. (1994). Sequential data assimilation with a nonlinear quasi-geostrophic model using Monte Carlo methods to forecast error statistics. *Journal of Geophysical Research*, *99*(C5), 10143. https://doi.org/10.1029/94JC00572

Evensen, G. (2003). The Ensemble Kalman Filter: theoretical formulation and practical implementation. *Ocean Dynamics*, *53*(4), 343–367. https://doi.org/10.1007/s10236-003-0036-9

Evensen, G. (2009a). *Data assimilation: the ensemble Kalman filter* (2nd ed). Dordrecht ; New York: Springer.

Evensen, G. (2009b). The ensemble Kalman filter for combined state and parameter estimation. *IEEE Control Systems*, *29*(3), 83–104. https://doi.org/10.1109/MCS.2009.932223

Fournier, T., Freymueller, J., & Cervelli, P. (2009). Tracking magma volume recovery at Okmok volcano using GPS and an unscented Kalman filter. *Journal of Geophysical Research*, *114*(B2). https://doi.org/10.1029/2008JB005837

Freymueller, J. T., & Kaufman, A. M. (2010). Changes in the magma system during the 2008 eruption of Okmok volcano, Alaska, based on GPS measurements. *Journal of Geophysical Research*, *115*(B12). https://doi.org/10.1029/2010JB007716

Got, J.-L., Carrier, A., Marsan, D., Jouanne, F., Vogfjörd, K., & Villemin, T. (2017). An analysis of the nonlinear magma-edifice coupling at Grimsvötn volcano (Iceland): NONLINEAR MAGMA-EDIFICE COUPLING. *Journal of Geophysical Research: Solid Earth*, *122*(2), 826–843. https://doi.org/10.1002/2016JB012905

Gregg, P. M., Le Mével, H., Zhan, Y., Dufek, J., Geist, D., & Chadwick, W. W. (2018). Stress Triggering of the 2005 Eruption of Sierra Negra Volcano, Galápagos. *Geophysical Research Letters*, *45*(24), 13,288-13,297. https://doi.org/10.1029/2018GL080393

Gregg, Patricia M., & Pettijohn, J. C. (2016). A multi-data stream assimilation framework for the assessment of volcanic unrest. *Journal of Volcanology and Geothermal Research*, *309*, 63–77. https://doi.org/10.1016/j.jvolgeores.2015.11.008

Gregg, P.M., de Silva, S. L., Grosfils, E. B., & Parmigiani, J. P. (2012). Catastrophic caldera-forming eruptions: Thermomechanics and implications for eruption triggering and maximum caldera dimensions on Earth. *Journal of Volcanology and Geothermal Research*, *241–242*, 1–12. https://doi.org/10.1016/j.jvolgeores.2012.06.009

Gregg, P.M., de Silva, S. L., & Grosfils, E. B. (2013). Thermomechanics of shallow magma chamber pressurization: Implications for the assessment of ground deformation data at active volcanoes. *Earth and Planetary Science Letters*, *384*, 100–108. https://doi.org/10.1016/j.epsl.2013.09.040

Grewal, M. S., & Andrews, A. P. (2008). *Kalman filtering: theory and practice using MATLAB* (3rd ed). Hoboken, N.J: Wiley.

Grosfils, E. B. (2007). Magma reservoir failure on the terrestrial planets: Assessing the importance of gravitational loading in simple elastic models. *Journal of Volcanology and Geothermal Research*, *166*(2), 47–75. https://doi.org/10.1016/j.jvolgeores.2007.06.007

Grosfils, E. B., McGovern, P. J., Gregg, P. M., Galgana, G. A., Hurwitz, D. M., Long, S. M., & Chestler, S. R. (2015). Elastic models of magma reservoir mechanics: a key tool for investigating planetary volcanism. *Geological Society, London, Special Publications*, *401*(1), 239–267. https://doi.org/10.1144/SP401.2

Julier, S., Uhlmann, J., & Durrant-Whyte, H. F. (2000). A new method for the nonlinear transformation of means and covariances in filters and estimators. *IEEE Transactions on Automatic Control*, *45*(3), 477–482. https://doi.org/10.1109/9.847726

Larsen, J., Neal, C., Webley, P., Freymueller, J., Haney, M., McNutt, S., et al. (2009). Eruption of Alaska Volcano Breaks Historic Pattern. *Eos, Transactions American Geophysical Union*, *90*(20), 173. https://doi.org/10.1029/2009EO200001

Larsen, J. F., Śliwiński, M. G., Nye, C., Cameron, C., & Schaefer, J. R. (2013). The 2008 eruption of Okmok Volcano, Alaska: Petrological and geochemical constraints on the subsurface magma plumbing system. *Journal of Volcanology and Geothermal Research*, *264*, 85–106. https://doi.org/10.1016/j.jvolgeores.2013.07.003

Le Mével, H., Gregg, P. M., & Feigl, K. L. (2016). Magma injection into a long-lived reservoir to explain geodetically measured uplift: Application to the 2007-2014 unrest episode at Laguna del Maule volcanic field, Chile: MAGMA INJECTION MODEL OF GEODETIC UPLIFT. *Journal of Geophysical Research: Solid Earth*, *121*(8), 6092–6108. https://doi.org/10.1002/2016JB013066

Long, S. M., & Grosfils, E. B. (2009). Modeling the effect of layered volcanic material on magma reservoir failure and associated deformation, with application to Long Valley caldera, California. *Journal of Volcanology and Geothermal Research*, *186*(3–4), 349–360. https://doi.org/10.1016/j.jvolgeores.2009.05.021

Lu, Z., Masterlark, T., & Dzurisin, D. (2005). Interferometric synthetic aperture radar study of Okmok volcano, Alaska, 1992-2003: Magma supply dynamics and postemplacement lava flow deformation: INSAR STUDY OF OKMOK VOLCANO. *Journal of Geophysical Research: Solid Earth*, *110*(B2). https://doi.org/10.1029/2004JB003148

Lu, Z., Dzurisin, D., Biggs, J., Wicks, C., & McNutt, S. (2010). Ground surface deformation patterns, magma supply, and magma storage at Okmok volcano, Alaska, from InSAR analysis: 1. Intereruption deformation, 1997–2008. *Journal of Geophysical Research*, *115*. https://doi.org/10.1029/2009JB006969

Mann, D., Freymueller, J., & Lu, Z. (2002). Deformation associated with the 1997 eruption of Okmok volcano, Alaska: DEFORMATION OF OKMOK VOLCANO, ALASKA. *Journal of Geophysical Research: Solid Earth*, *107*(B4), ETG 7-1-ETG 7-12. https://doi.org/10.1029/2001JB000163

Martí, J., López, C., Bartolini, S., Becerril, L., & Geyer, A. (2016). Stress Controls of Monogenetic Volcanism: A Review. *Frontiers in Earth Science*, *4*. https://doi.org/10.3389/feart.2016.00106

McGuire, J. J., & Segall, P. (2003). Imaging of aseismic fault slip transients recorded by dense geodetic networks. *Geophysical Journal International*, *155*(3), 778–788. https://doi.org/10.1111/j.1365-246X.2003.02022.x

McTigue, D. F. (1987). Elastic stress and deformation near a finite spherical magma body: Resolution of the point source paradox. *Journal of Geophysical Research*, *92*(B12), 12931. https://doi.org/10.1029/JB092iB12p12931

Miller, T. P., & Smith, R. L. (1987). Late Quaternary caldera-forming eruptions in the eastern Aleutian arc, Alaska, 5.

Miyazaki, S., Segall, P., Fukuda, J., & Kato, T. (2004). Space time distribution of afterslip following the 2003 Tokachi-oki earthquake: Implications for variations in fault zone frictional properties: AFTERSLIP FOLLOWING THE 2003 TOKACHI-OKI EARTHQUAKE. *Geophysical Research Letters*, *31*(6), n/a-n/a. https://doi.org/10.1029/2003GL019410

Mogi, K. (1958). Relations between the eruptions of various volcanoes and the deformations of the ground surfaces around them. *Bulletin of the Earthquake Research Institude*, *36*, 99–134.

Natvik, L.-J., & Evensen, G. (2003). Assimilation of ocean colour data into a biochemical model of the North Atlantic. *Journal of Marine Systems*, *40–41*, 127–153. https://doi.org/10.1016/S0924-7963(03)00016-2

Nooner, S. L., & Chadwick, W. W. (2016). Inflation-predictable behavior and co-eruption deformation at Axial Seamount. *Science*, *354*(6318), 1399–1403. https://doi.org/10.1126/science.aah4666

Rubin, A. M. (1995). Propagation of Magma-Filled Cracks. *Annual Review of Earth and Planetary Sciences*, *23*(1), 287–336.

Segall, P. (2013). Volcano deformation and eruption forecasting. *Geological Society, London, Special Publications*, *380*(1), 85–106. https://doi.org/10.1144/SP380.4

Segall, P., & Matthews, M. (1997). Time dependent inversion of geodetic data. *Journal of Geophysical Research: Solid Earth*, *102*(B10), 22391–22409. https://doi.org/10.1029/97JB01795

Seiler, A., Evensen, G., Skjervheim, J.-A., Hove, J., & Vabo, J. G. (2009). Advanced Reservoir Management Workflow Using an EnKF Based Assisted History Matching Method. In *SPE Reservoir Simulation Symposium*. The Woodlands, Texas: Society of Petroleum Engineers. https://doi.org/10.2118/118906-MS

Sparks, R. S. J. (2003). Forecasting volcanic eruptions. *Earth and Planetary Science Letters*, *210*(1–2), 1–15. https://doi.org/10.1016/S0012-821X(03)00124-9

Voight, B., Hoblitt, R. P., Clarke, A. B., Lockhart, A. B., Miller, A. D., Lynch, L., & McMahon, J. (1998). Remarkable cyclic ground deformation monitored in real-time on Montserrat, and its use in eruption forecasting. *Geophysical Research Letters*, *25*(18), 3405–3408. https://doi.org/10.1029/98GL01160

Wilson, G. W., Özkan-Haller, H. T., Holman, R. A., Haller, M. C., Honegger, D. A., & Chickadel, C. C. (2014). Surf zone bathymetry and circulation predictions via data assimilation of remote sensing observations. *Journal of Geophysical Research: Oceans*, *119*(3), 1993–2016. https://doi.org/10.1002/2013JC009213

Yang, X.-M., Davis, P. M., & Dieterich, J. H. (1988). Deformation from inflation of a dipping finite prolate spheroid in an elastic half-space as a model for volcanic stressing. *Journal of Geophysical Research: Solid Earth*, *93*(B5), 4249–4257. https://doi.org/10.1029/JB093iB05p04249

Zhan, Y., & Gregg, P. M. (2017). Data assimilation strategies for volcano geodesy. *Journal of Volcanology and Geothermal Research*, *344*, 13–25. https://doi.org/10.1016/j.jvolgeores.2017.02.015

AGU PUBLICATIONS

Geophysical Research Letters

Supporting Information for

Hindcasting magma reservoir stability preceding the 2008 eruption of Okmok, Alaska

J. A. Albright[1], P. M. Gregg[1], Z. Lu[2], and J. T. Freymueller[3]

[1]Department of Geology, University of Illinois at Urbana-Champaign, IL, USA [2]Huffington Department of Earth Sciences, Southern Methodist University, Dallas, TX, USA [3]Department of Earth and Environmental Sciences, Michigan State University, Lansing, MI, USA

Contents of this file

Introduction

The beginning of this document contains a more complete explanation of the methods used in the main article, complete with associated figures, equations, and tables. It goes on to show comparisons between model predictions and all available InSAR and GPS data, for which there was otherwise insufficient space. The final sections record ancillary experiments referenced in the main text done to assess the performance of each individual dataset, along with the influence of rheology on our results.

S1. Supplementary Methods

In this section the computational methods for finite element model setup, Ensemble Kalman Filter (EnKF) data assimilation approach, and mechanical failure criterion are described.

S1.1. Finite Element Model Setup

We follow previously benchmarked approaches for a pressurized magma chamber in an elastic medium utilizing COMSOL Multiphysics 5.3 (e.g. Grosfils (2007), Gregg et al. (2012)). Our model uses a linear elastic rheology and solves for stress and strain at each point in the model space due to an applied stress at the magma chamber boundary (Fig. S1). All variables and parameter values are provided in Tables S1 and S2 at the end of this document. Our experiments assume a Young's Modulus of 75 GPa and a Poisson's ratio of 0.25, with the exception of one trial that uses a Young's Modulus of 50 GPa, as detailed in section S4 below.

S1.2. Ensemble Kalman Filter Data Assimilation Approach

Statistical data assimilation is a class of model-data fusion methods that combines models of a dynamic system with observations to evaluate how the system is evolving. In this investigation we utilize the Ensemble Kalman Filter (EnKF), which has been recently adapted for volcano applications (Patricia M. Gregg & Pettijohn, 2016; Zhan & Gregg, 2017). The EnKF uses a Markov Chain Monte Carlo (MCMC) approach to estimate Kalman filter covariance while tracking model state variables and parameters to provide model updates and forecasts (Evensen, 1994, 2003, 2009a, 2009b). In application, hundreds of models are propagated forward in time in an "ensemble" which is updated at specific time steps when data are available. The EnKF has a proven track record for highly nonlinear problems and forecasting applications in a variety of fields such as hydrology, oil reservoir modeling, climatology, ecosystem modeling, weather forecasting, and physical oceanography (Allen et al., 2003; Brusdal et al., 2003; Evensen, 1994, 2003; Natvik & Evensen, 2003; Seiler et al., 2009; Wilson et al., 2014).

Although other iterations of Kalman Filtering such as the Extended Kalman Filter (EKF) and the Unscented Kalman Filter (UKF) have been successfully applied to geodetic data (Aoki et al., 1999; Fournier et al., 2009; McGuire & Segall, 2003; Miyazaki et al., 2004; Segall & Matthews, 1997), these versions require explicit derivations of the covariance matrix and are therefore constrained to use with well-defined analytical models. One drawback of this approach, however, is that such models are only capable of predicting certain eruption triggering mechanisms, typically the presence of a critical overpressure. In contrast, the EnKF is compatible with more complex FEMs, which in turn can track both the pressure within the reservoir and the stress state of the surrounding rock, allowing our approach to test additional eruption triggers.

In this study we use the assimilation approach of Zhan & Gregg (2017) (Fig. S2), with the following specifications and adjustments. To ensure computational feasibility, the GPS data were downsampled in time to 10-day averaged bins, and the InSAR data were downsampled in space through a quadtrees algorithm. The uncertainty values used for the GPS data within the EnKF were taken from estimated instrumental errors included as part of the original daily solution dataset, whereas a constant 5 mm error was assumed for the InSAR. In order to prevent catastrophic divergence of the ensemble, the minimum standard deviation in any given parameter was restricted to 5% of its mean value. If a parameter narrowed beyond this limit on any given iteration, its values were redistributed around the same mean ±10%. Similarly, if the parameters of any single ensemble member represented a physically impossible or unfeasible model state, such as having a negative radius or a reservoir that breached the surface, those particular values were removed and replaced with a random value from the initial distribution of the given parameter.

These experiments were conducted on a iMac Retina 5K with 32 Gb of memory and a 3.2 GHz Intel Core i5 processor using COMSOL Multiphysics version 5.3 with LiveLink to Matlab R2017a. Computational runtimes are given in Table S3 at the end of this document.

S1.3. Estimating Failure

The presented approach investigates three failure criteria to evaluate the stability of the Okmok magma system in the lead up to the 2008 eruption: (1) Mohr-Coulomb failure; (2) magma reservoir overpressure; and (3) tensile failure.

Mohr-Coulomb failure is evaluated as:

$$|\tau| - |\sigma_n \tan \varphi| \geq C \qquad (1)$$

where σ_n is normal stress, τ is shear stress, *C* is cohesion, and φ is internal angle of friction. Normal and shear stressed are defined using the principal stresses as:

$$\tau = \frac{\sigma_3 - \sigma_1}{2}\cos\varphi \quad (2)$$

$$\sigma_n = \frac{\sigma_3 + \sigma_1}{2} - \frac{\sigma_3 - \sigma_1}{2}\sin\varphi \quad (3)$$

where σ_1 is the least compressive stress and σ_3 is the most compressive. Following the conventions of COMSOL, tension is positive and compression is negative throughout this paper. As the failure envelope is not well constrained, the model tracks a number of cohesions from 0 MPa to 25 MPa.

Fig. S3 illustrates the evolution of Mohr-Coulomb failure in the lead up to the 2008 eruption. Mohr-Coulomb failure did not appear to capture the evolution of the system in the lead up to the eruption, but likely has implications for seismicity rate that should be evaluated in future investigations.

Magma reservoir overpressure *dP* is described as the pressure applied along the reservoir boundary in excess of lithostatic confining pressure. This relationship can be described as:

$$P = -dP + \rho_r g z \quad (4)$$

where P is the total pressure exerted along the model boundary, ρ_r is the density of the host rock, *g* is gravitational acceleration, and *z* is depth below the surface expressed as a negative value. Overpressure-driven failure is defined as occurring when

$$dP \geq 10 - 40\ MPa \quad (5)$$

as shown in previous models investigating dike initiation and propagation (Rubin, 1995). We define tensile failure along the reservoir wall to occur locally defined as

$$\sigma_1 \geq \sigma_T \quad (6),$$

where σ_T is the positive tensile strength of the host rock, which typically ranges from 1 - 20 MPa for crustal rocks (Cho et al., 2003). As an exact value for Okmok is unknown, we evaluate a range of tensile failure thresholds to determine which may be most appropriate for this system.

S2. Full data comparisons for combined assimilation

Figs. S4-S6 compare the continuous GPS, campaign GPS, and InSAR data used in this study with the observations predicted by the EnKF data assimilation. Fig. 2 in the main text contains a selection of these data. Fig. S7 plots the root mean squared error (RMSE) of each dataset over the course of the joint assimilation, the single-dataset assimilations (see S3, below), and the lowered Young's Modulus joint assimilation (see S4, below).

S3. GPS-only and InSAR-only EnKF assimilation results

In addition to the combined GPS+InSAR model runs presented in the main text, experiments were conducted using GPS and InSAR alone. GPS-only data fits and parameter estimations are provided in Figs. S8-S9 and S10 respectively. Fig. S11 provides an evaluation of failure as the model evolves. Figs. S12 and S13 provide data fits and parameter estimations for the InSAR-only data assimilations runs. The predicted failure evolution for the InSAR only run is provided in Figure S14.

A major outcome from the single-technique GPS and InSAR experiments is that both failed to capture an increase in eruption likelihood coinciding with the 2008 event. For the GPS-only assimilation, for instance, failure is over-predicted. Regardless of tensile strength, over 90% of models begin to predict tensile failure as early as 2006, well before the observed period of pre-eruptive deformation in 2008. On the other hand, the InSAR-only assimilation predicts absolutely no failure, even immediately before the eruption.

We hypothesize that this mismatch is due to the different sensitivities of each dataset to certain reservoir parameters. While the reservoir depth is fairly consistent between the joint and GPS-only assimilations, the predicted half-width is significantly larger in the absence of the InSAR data. A wider reservoir has greater stress concentrations on the tips and is therefore produces tensile failure more easily. While the InSAR-only run also produces a significantly wider reservoir than the joint assimilation, the pressure within the reservoir becomes much lower, inhibiting any failure. In this instance the combined approach was necessary to provide an accurate hindcast of the eruption, but this result does not imply that future investigations using one method alone will not work.

S4. Reduced Young's Modulus assimilation results

In order to evaluate the impact of rheology on the assimilation process, an additional experiment was conducted in which the modeled Young's Modulus was set to 50 GPa, down from 75 GPa as used in the rest of the study. Figures S15-S16 compare the model predictions against GPS data, while Figure S17 compares against InSAR data. Figure S18 shows the evolution of variables throughout the assimilation, while Figure S19 evaluates the likelihood of mechanical failure. Figure S20 compares the maximum tensile stress measured along the reservoir wall between all assimilations.

The change in elastic moduli has a significant impact on the model predictions, most notably in a ~20 MPa lower net pressure change (dP) and a nearly complete absence of mechanical failure immediately pre-eruption. With a weaker rheology, less stress is required to produce the observed amount of strain (i.e. ground deformation) and the modeled failure criteria are therefore not met. These results suggest that a Young's Modulus of 50 MPa may be unable to account for the deformation and eruptive history at Okmok. Moreover, this conclusion highlights the importance of conducting hind-casts of previous eruptions, since such a process allowed model parameters such as rheology to be adjusted based on the presence or absence of observed behavior.

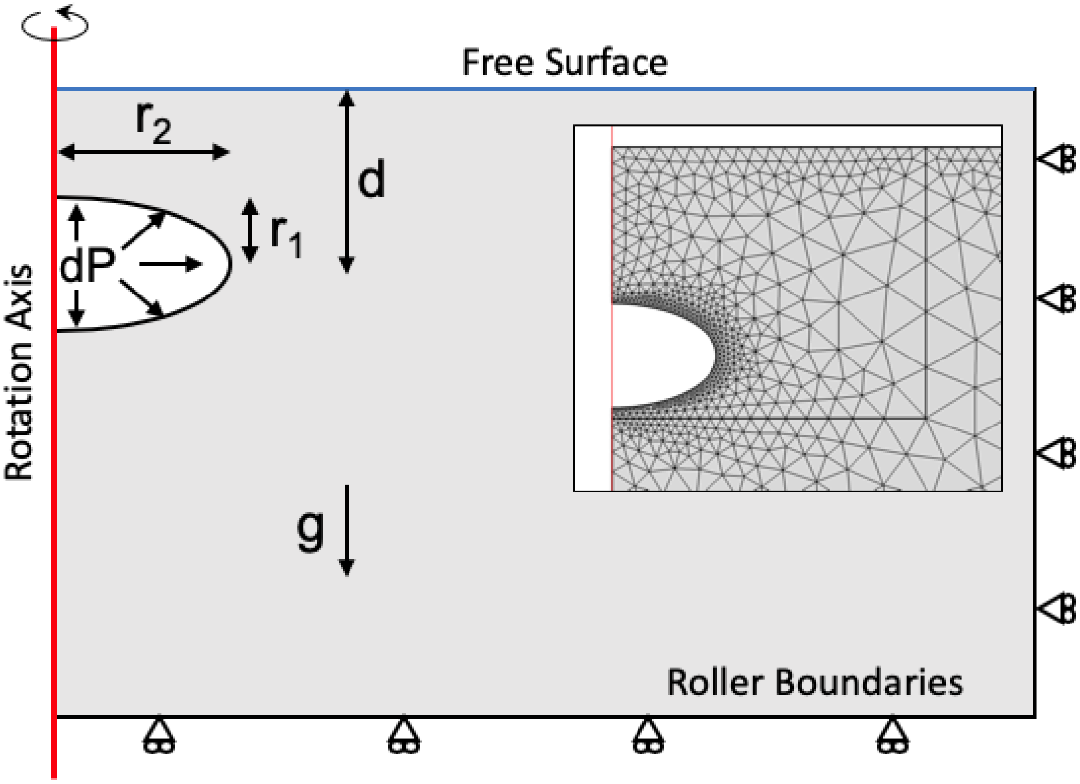

Figure S1. Finite Element Model Setup. The finite element approach assumes a two-dimensional, axissymmetric, linearly elastic domain. The top of the model is assumed to be a free surface, and the side and bottom of the domain have imposed roller boundary conditions. The domain is gravitationally loaded. An instantaneous pressure source is assumed at the magma chamber boundary.

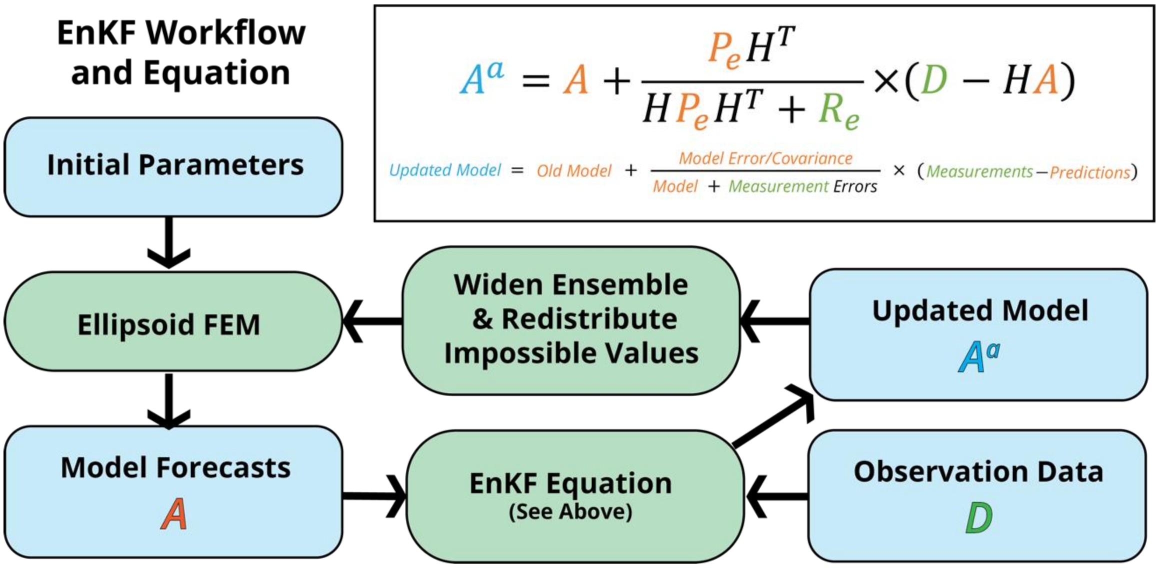

Figure S2. The EnKF workflow used in this study. Inset: EnKF update equation, with simplified descriptions of each matrix used. The matrices are more explicitly defined and explained in Zhan & Gregg (2017).

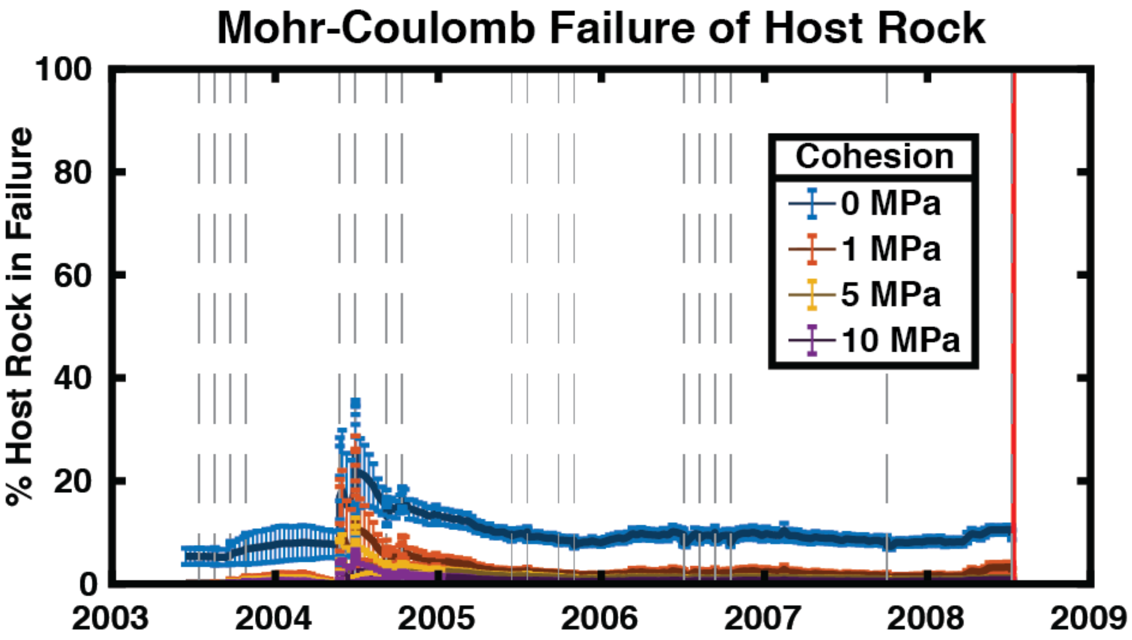

Figure S3. The evolution of model predicted Mohr-Coulomb failure in the lead up to the 2008 eruption assuming 4 different cohesions for the surrounding host rock Percentages given are relative to a rectangular area in the model space that reaches from the surface to 200 m below the reservoir and from the rotation axis to a distance of 3 times the half-width of the reservoir.

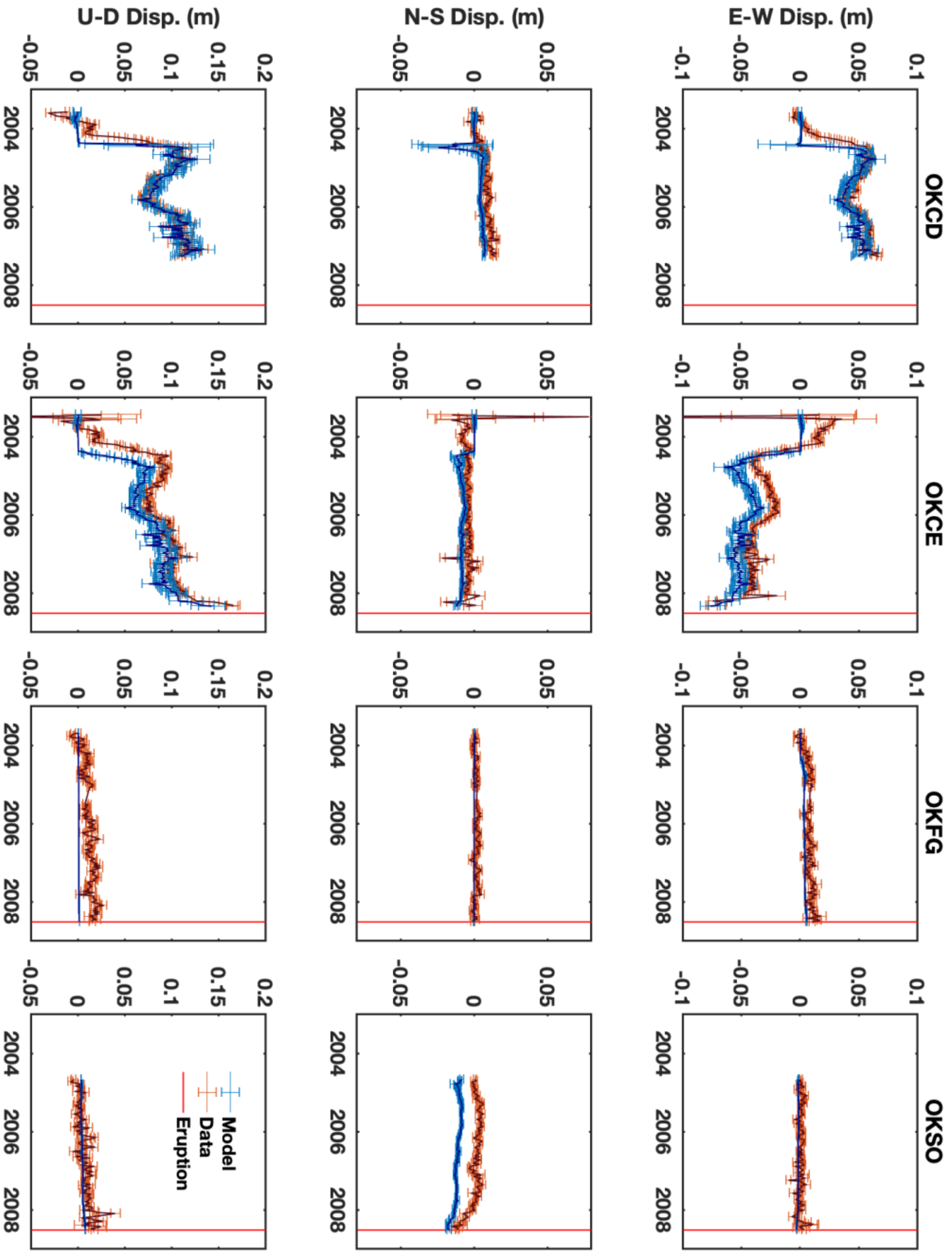

Figure S4. GPS Fit for continuous instruments the joint hindcast showing all four continuous sites that were used.

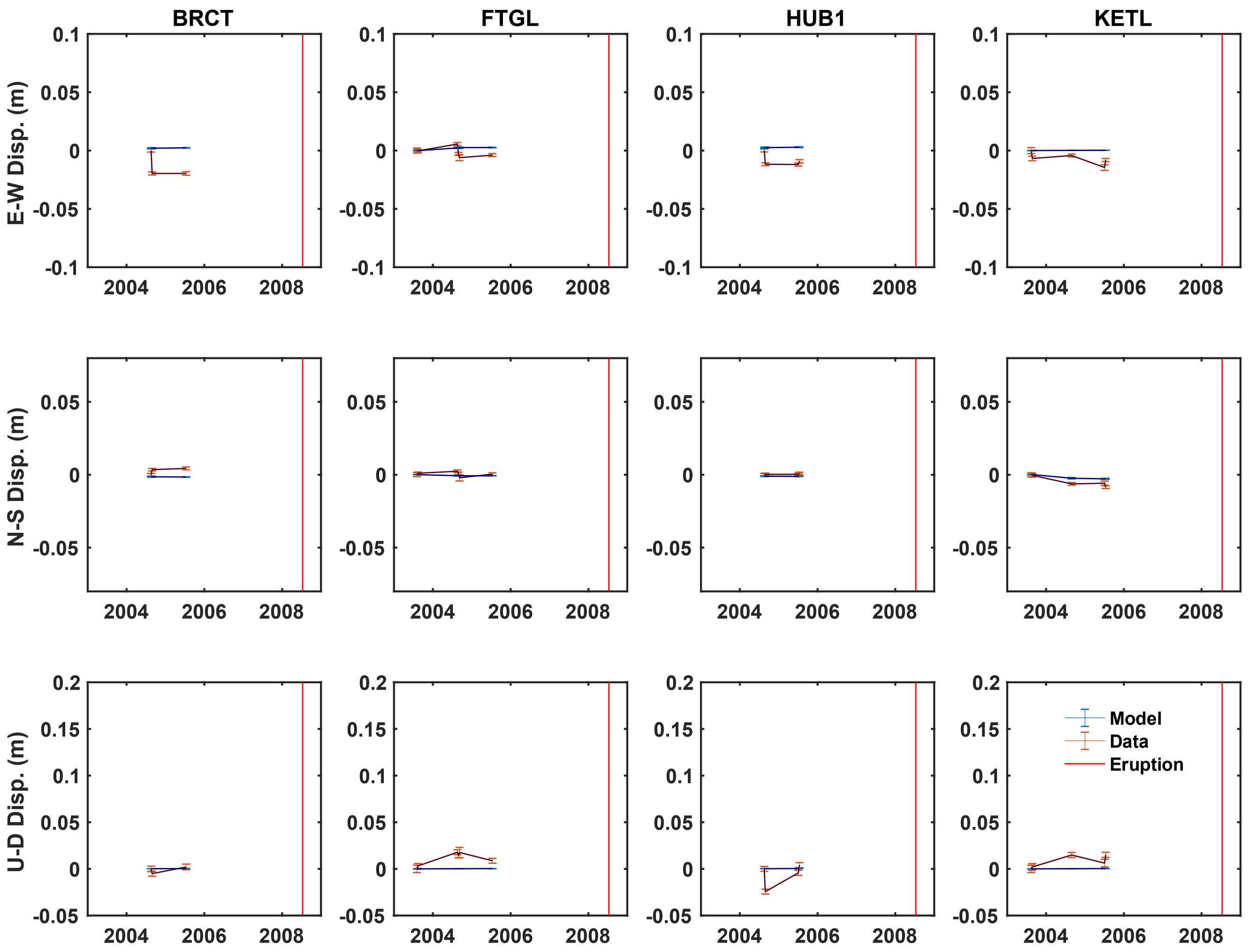
BRCT
FTGL
HUB1
KETL
E-W Disp. (m)
N-S Disp. (m)
U-D Disp. (m)
0.1
0.05
0
-0.05
-0.1
0.2
0.15
2004
2006
2008
Model
Data
Eruption

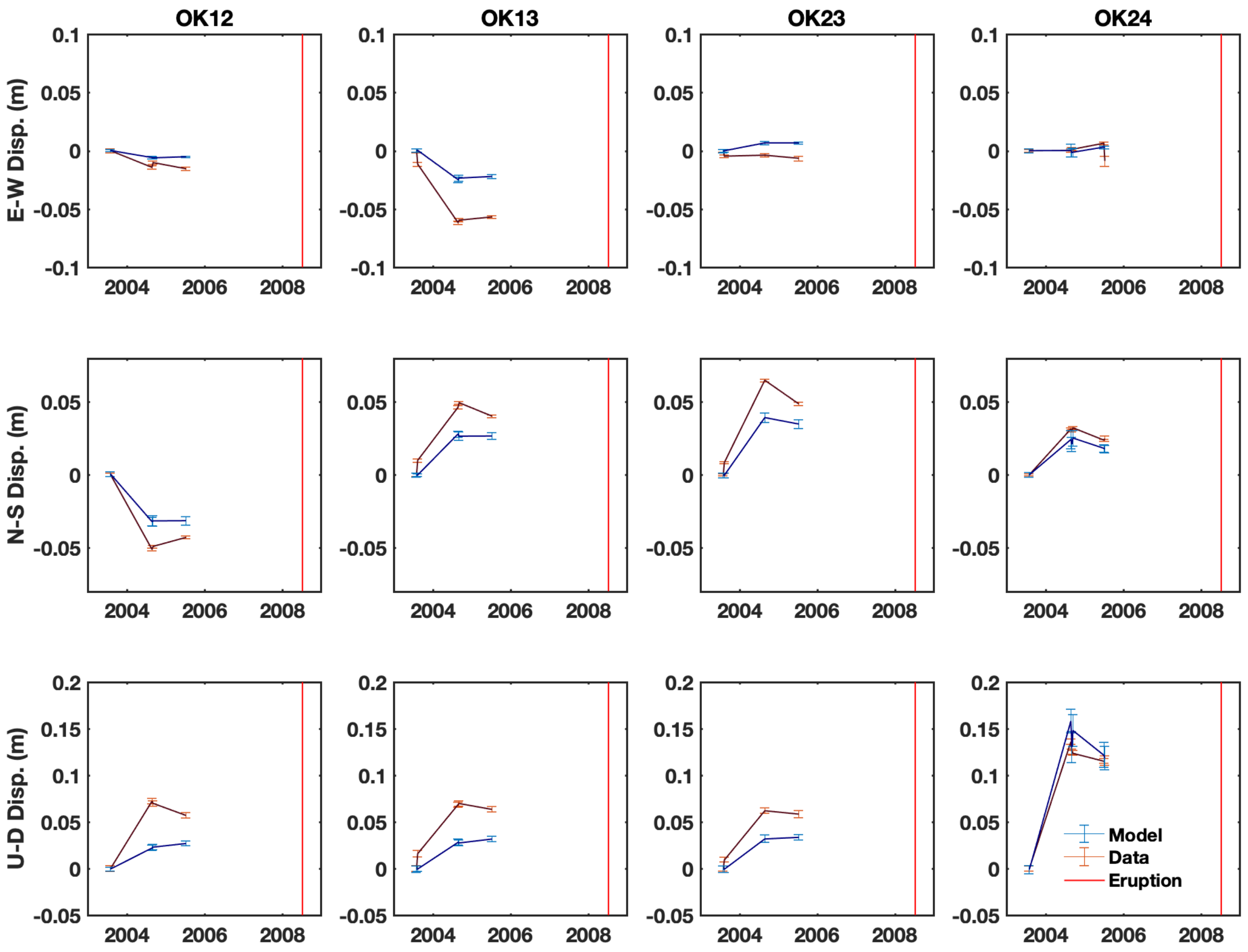
OK12
OK13
OK23
OK24
E-W Disp. (m)
N-S Disp. (m)
U-D Disp. (m)
0.1
0.05
0
-0.05
-0.1
0.2
0.15
2004
2006
2008
Model
Data
Eruption

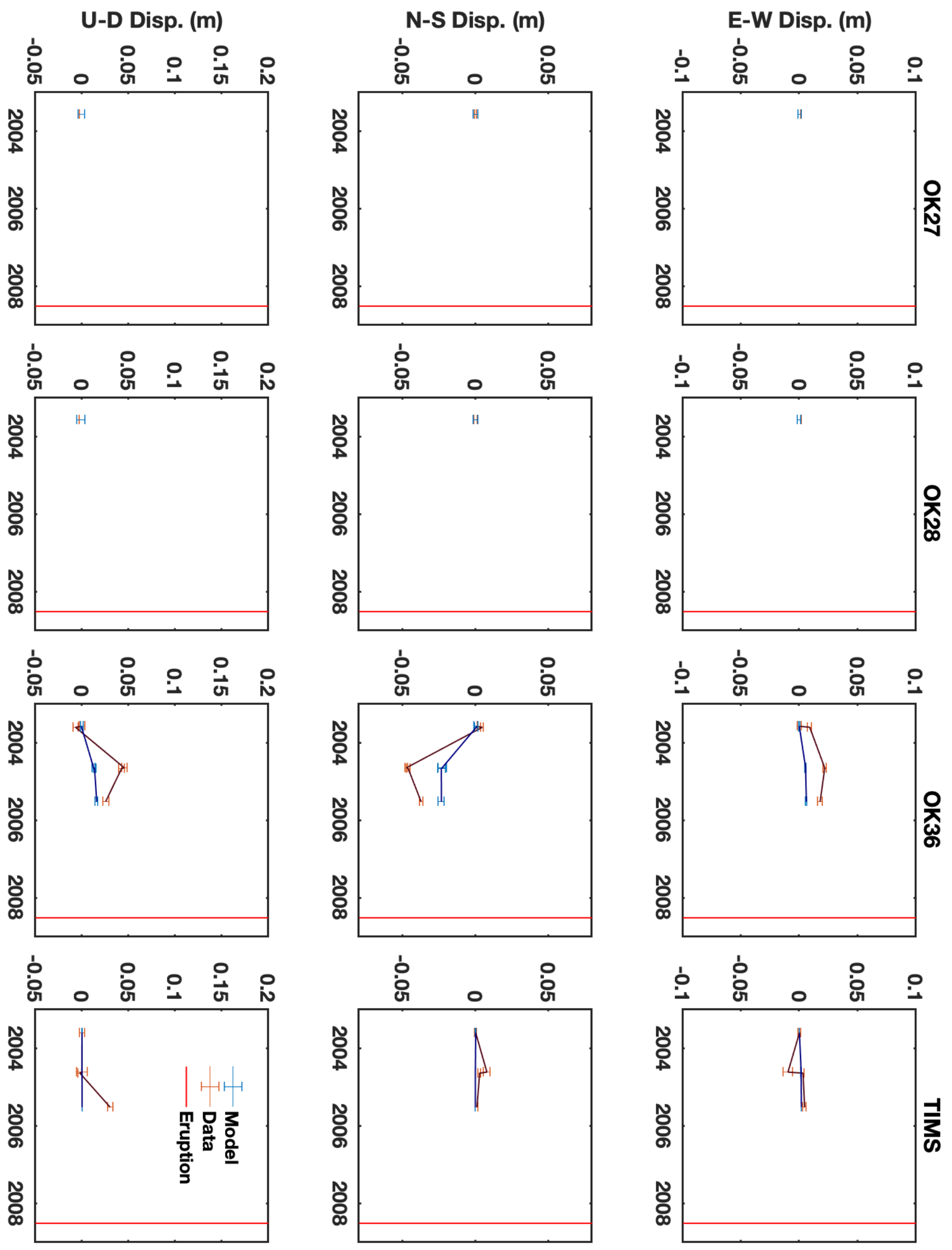

Figure S5. (3 pages) GPS Fit for campaign sites in the joint hindcast showing all sites that were used.

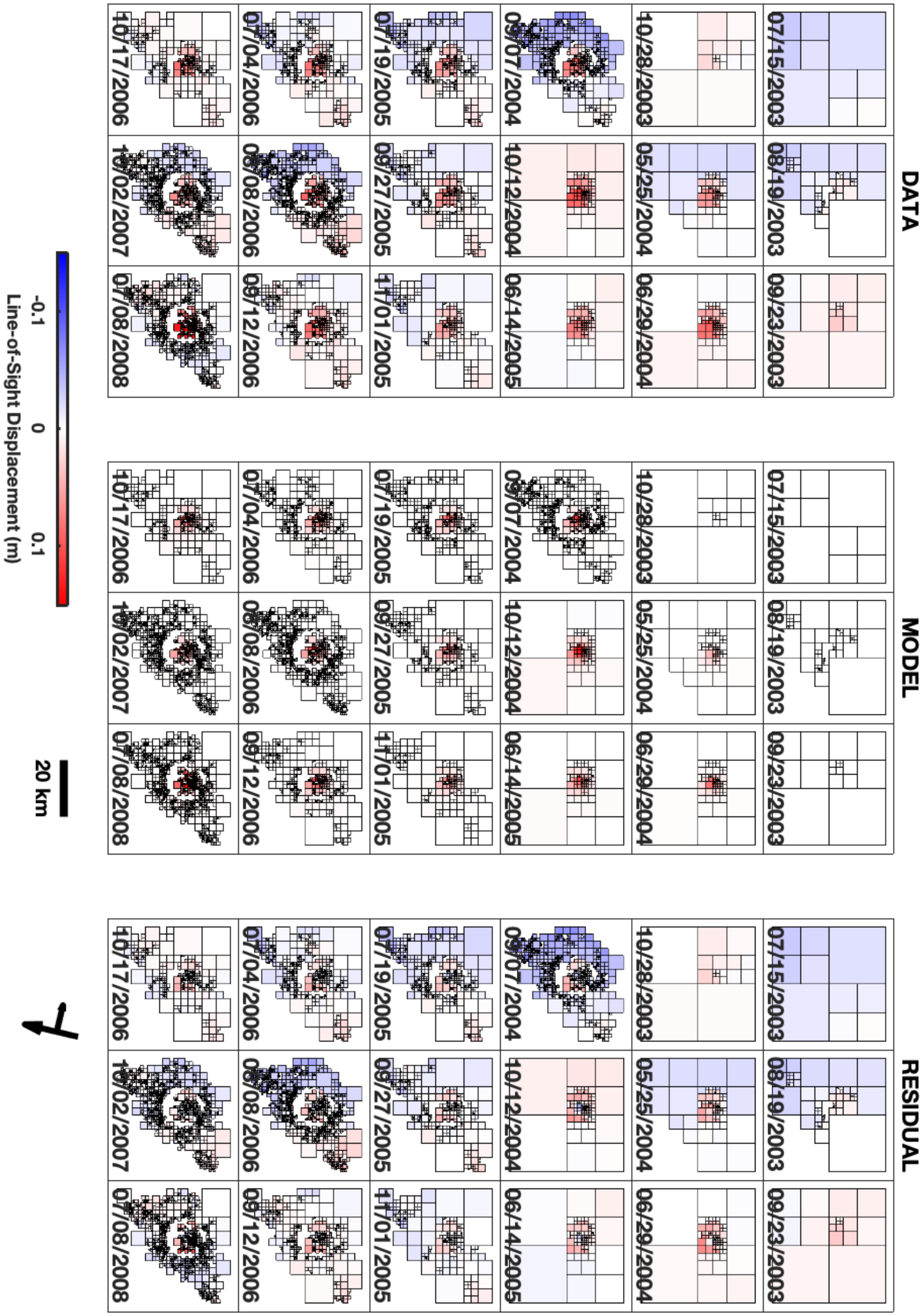

Figure S6. InSAR fit for every InSAR image used in the joint hindcast. Cumulative deformation from initial SAR image on 06/10/2003.

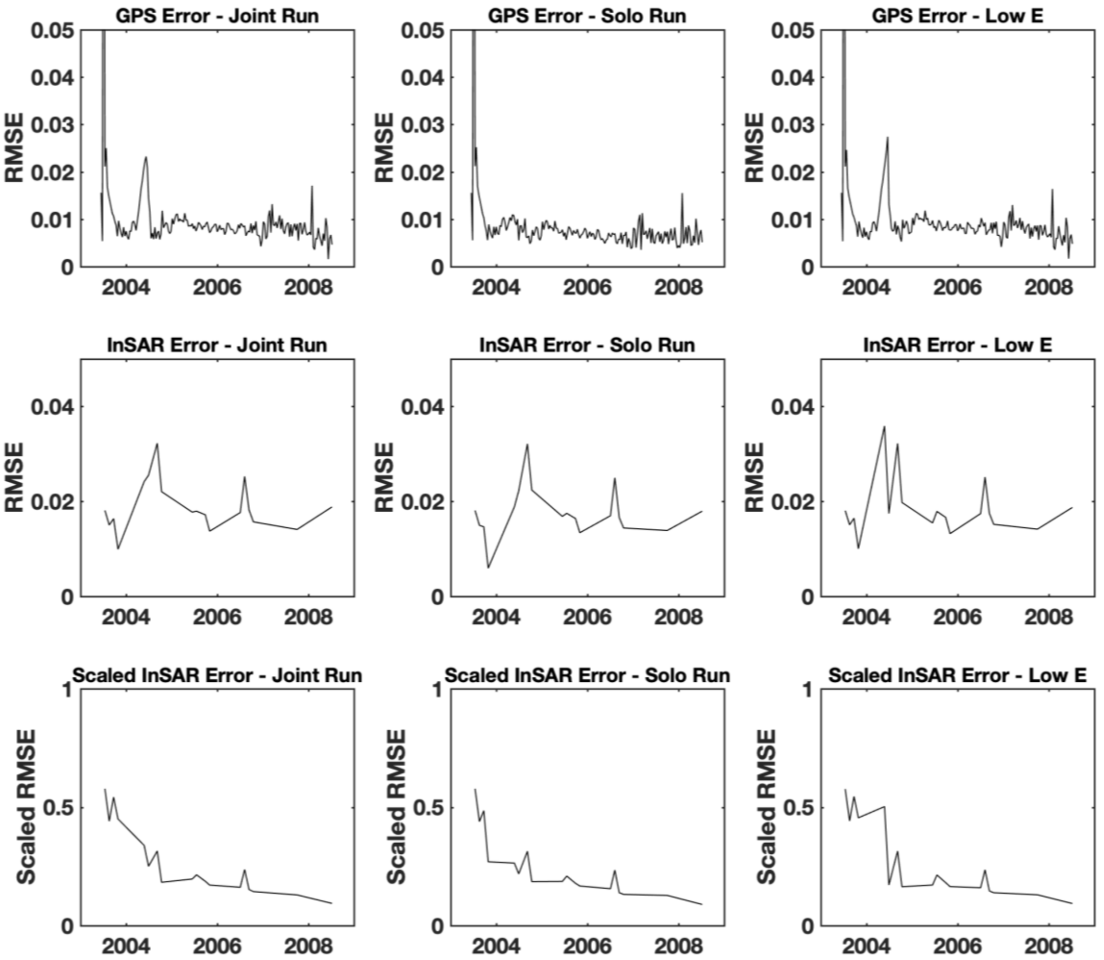

Figure S7. Root mean square error (RMSE) calculations comparing EnKF predictions with measured GPS and InSAR deformation for Joint, GPS-only, InSAR-only, and reduced Young's Modulus assimilations. Although the InSAR RMSE does not appear to substantially decrease over the assimilation, the observed error becomes smaller relative to the total deformation in the system, as shown in the bottom three graphs.

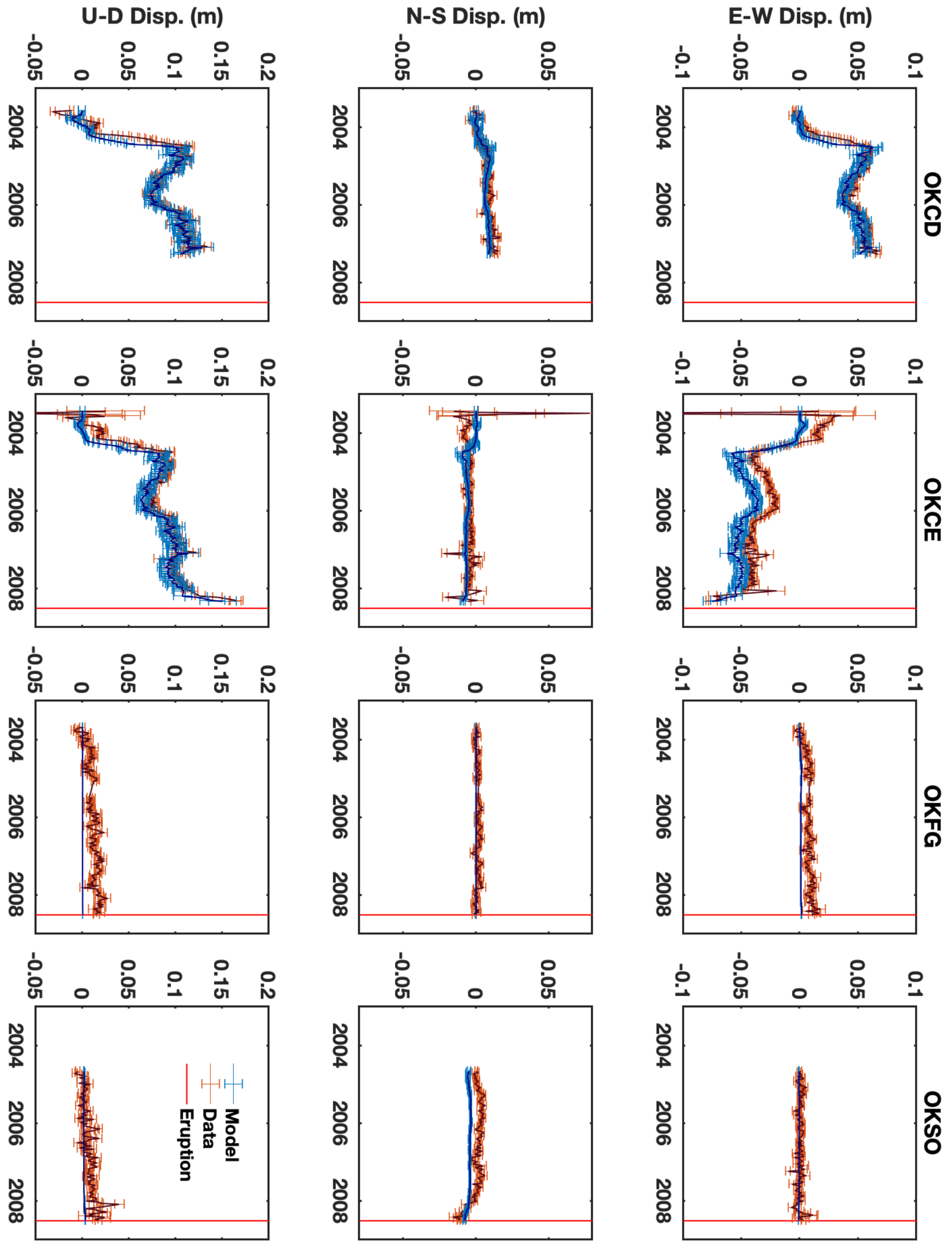

Figure S8. GPS fit for continuous sites in the GPS-only assimilation.

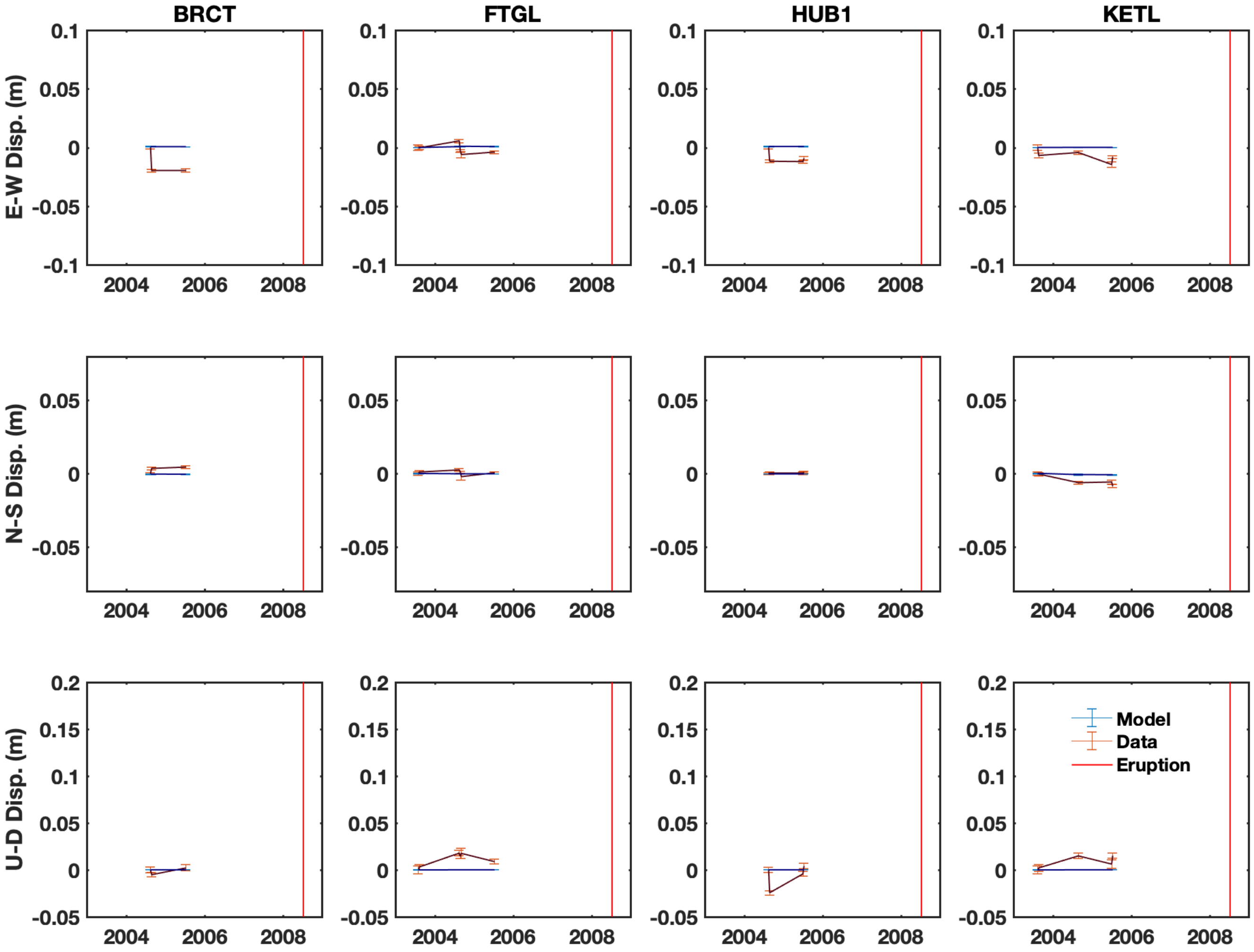BRCT
FTGL
HUB1
KETL
E-W Disp. (m)
N-S Disp. (m)
U-D Disp. (m)
0.1
0.05
0
-0.05
-0.1
0.2
0.15
2004
2006
2008
Model
Data
Eruption

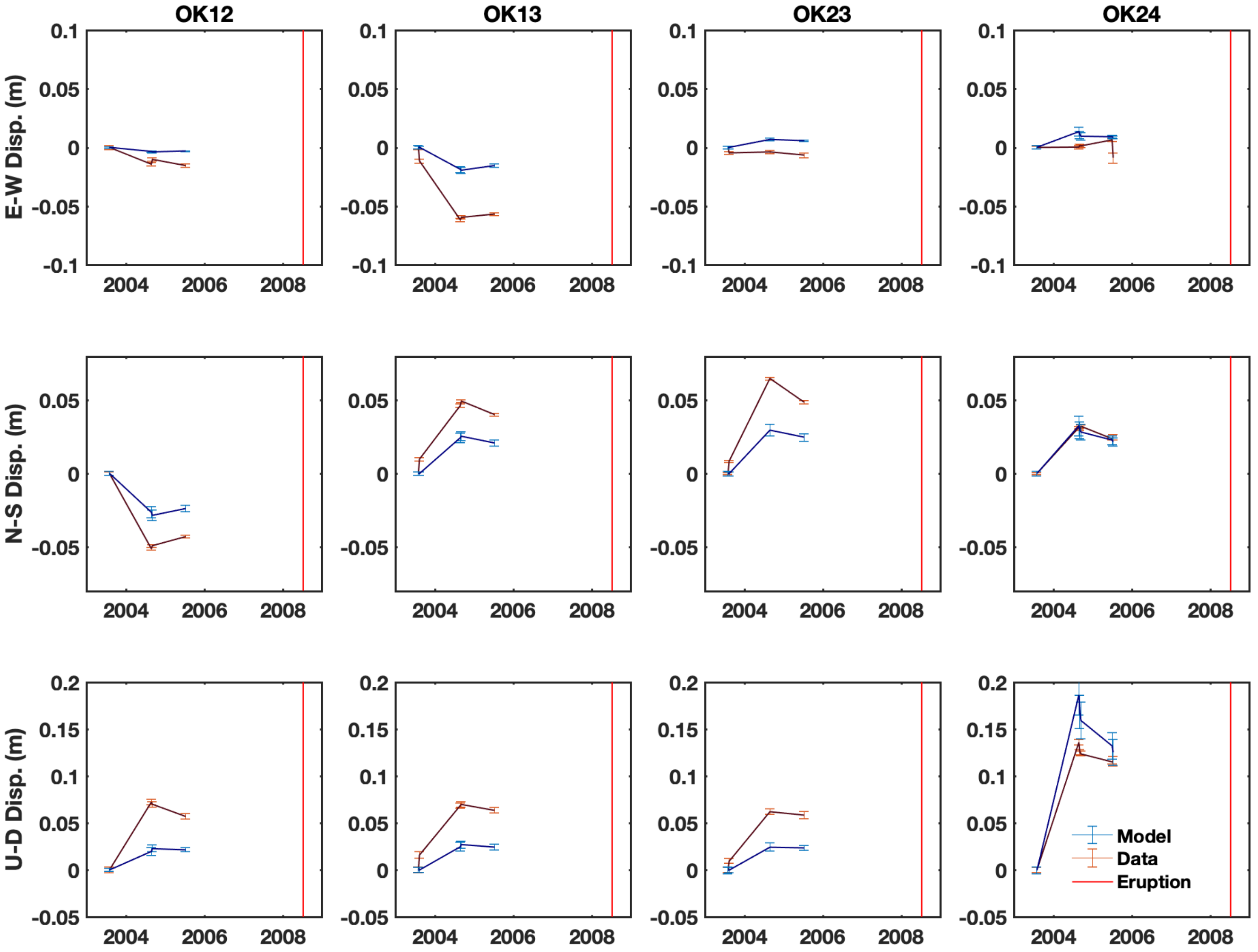OK12
OK13
OK23
OK24
E-W Disp. (m)
N-S Disp. (m)
U-D Disp. (m)
0.1
0.05
0
-0.05
-0.1
0.2
0.15
2004
2006
2008
Model
Data
Eruption

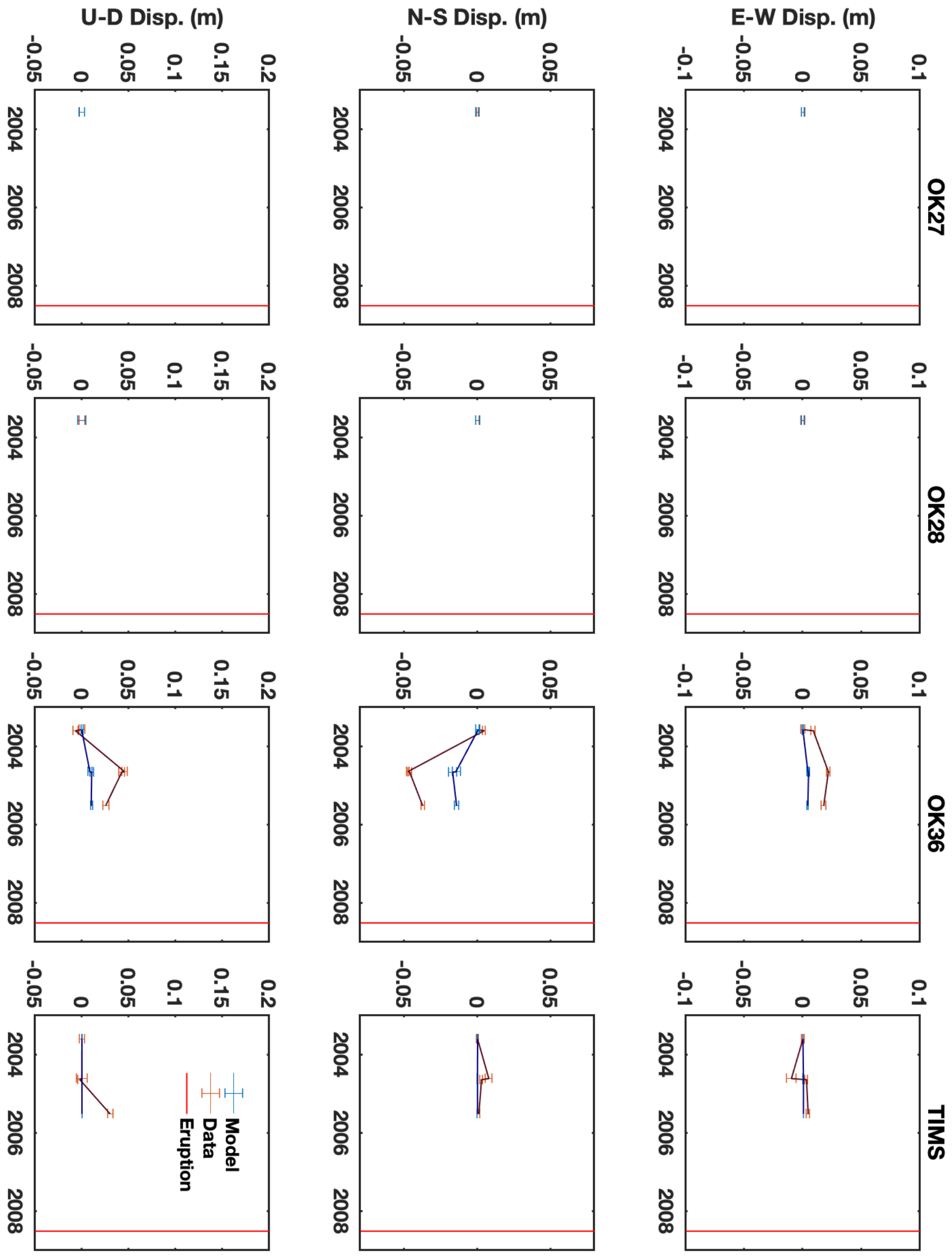

Figure S9. (3 Pages) GPS fit for campaign sites in the GPS-only assimilation.

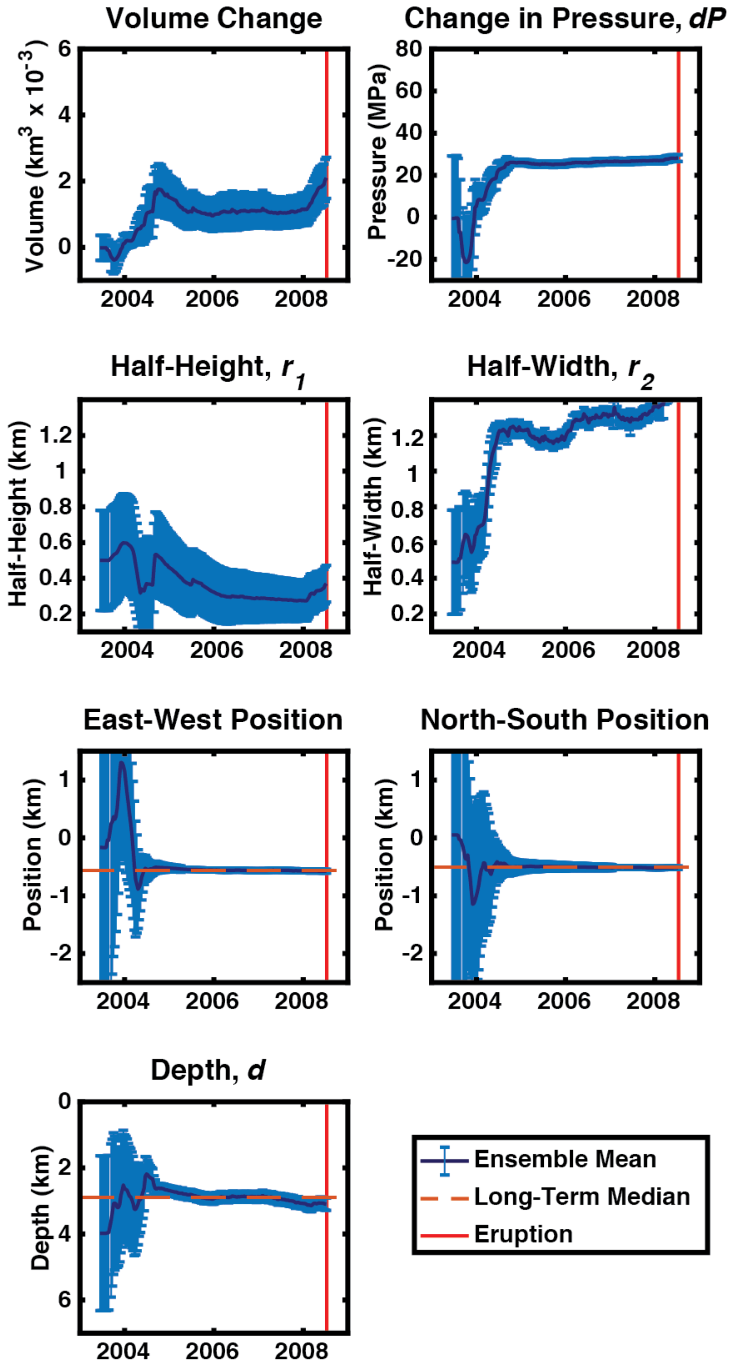

Figure S10. EnKF predictions of model variables for the GPS-only assimilation. Uncertainty given by twice the observed standard deviation in each parameter (N = 300).

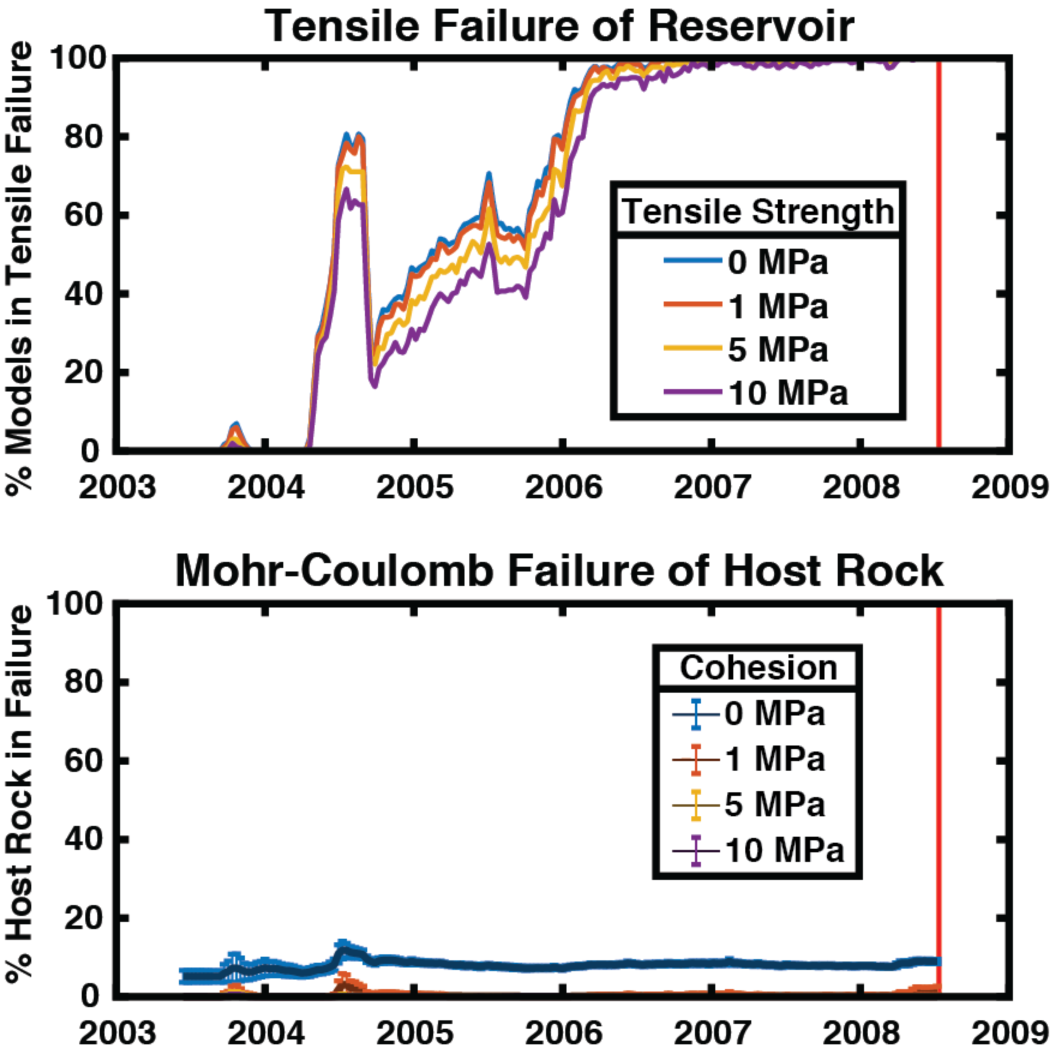

Figure S11. Predicted rates of tensile (top) and Mohr-Coulomb failure (bottom) for the GPS-only assimilation.

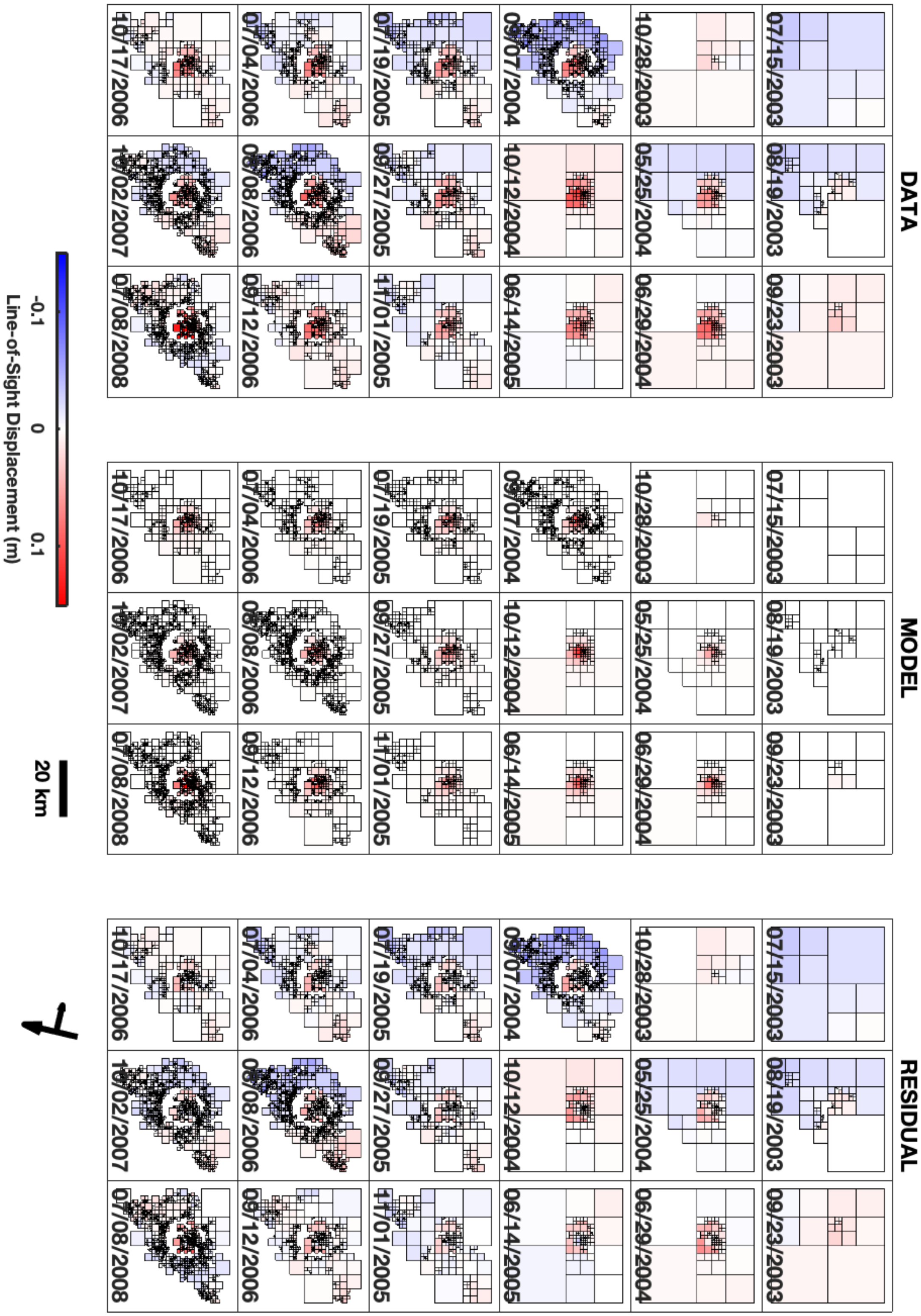

Figure S12. InSAR fit for every InSAR image used in the InSAR-only assimilation. Cumulative deformation from initial SAR image on 06/10/2003

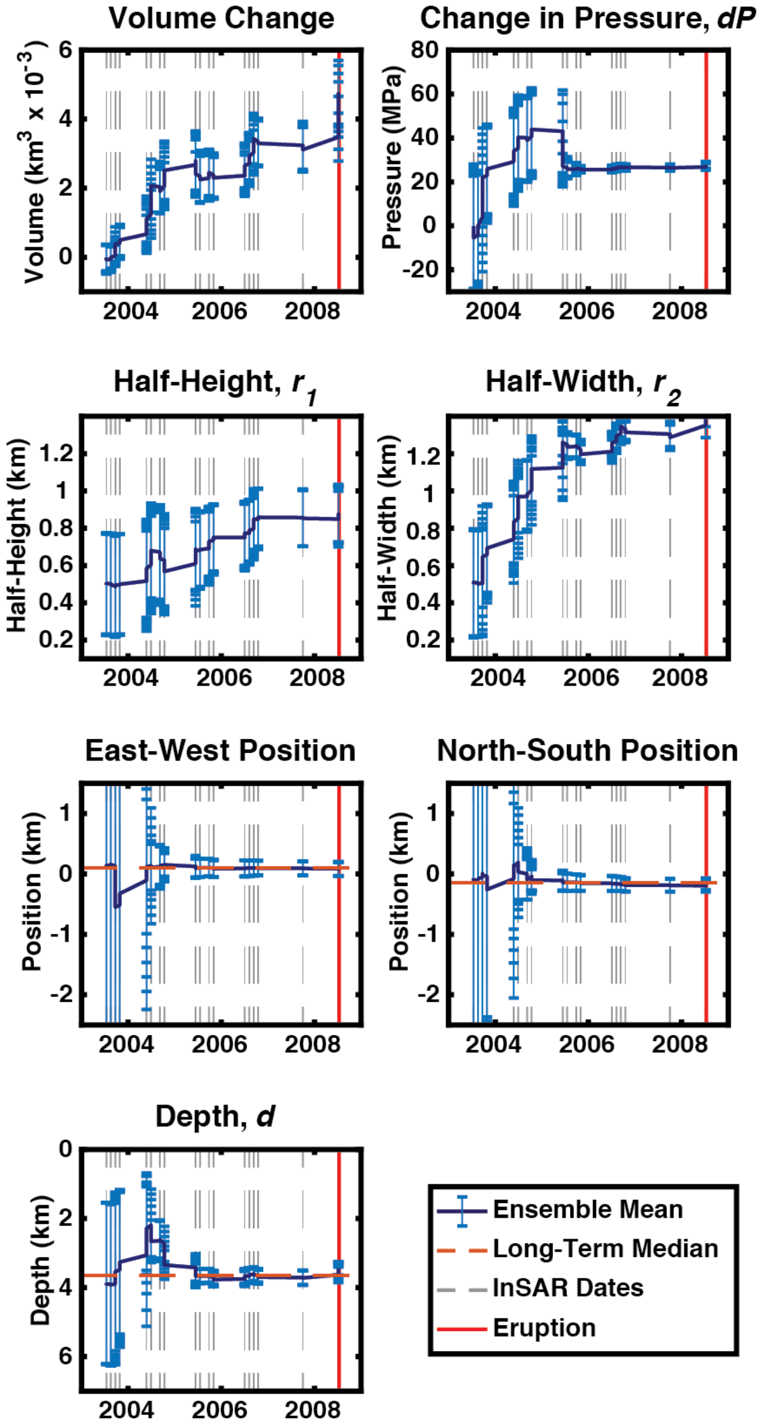

Figure S13. EnKF predictions of model variables for the InSAR-only assimilation. Uncertainty given by twice the observed standard deviation in each parameter (N = 300)

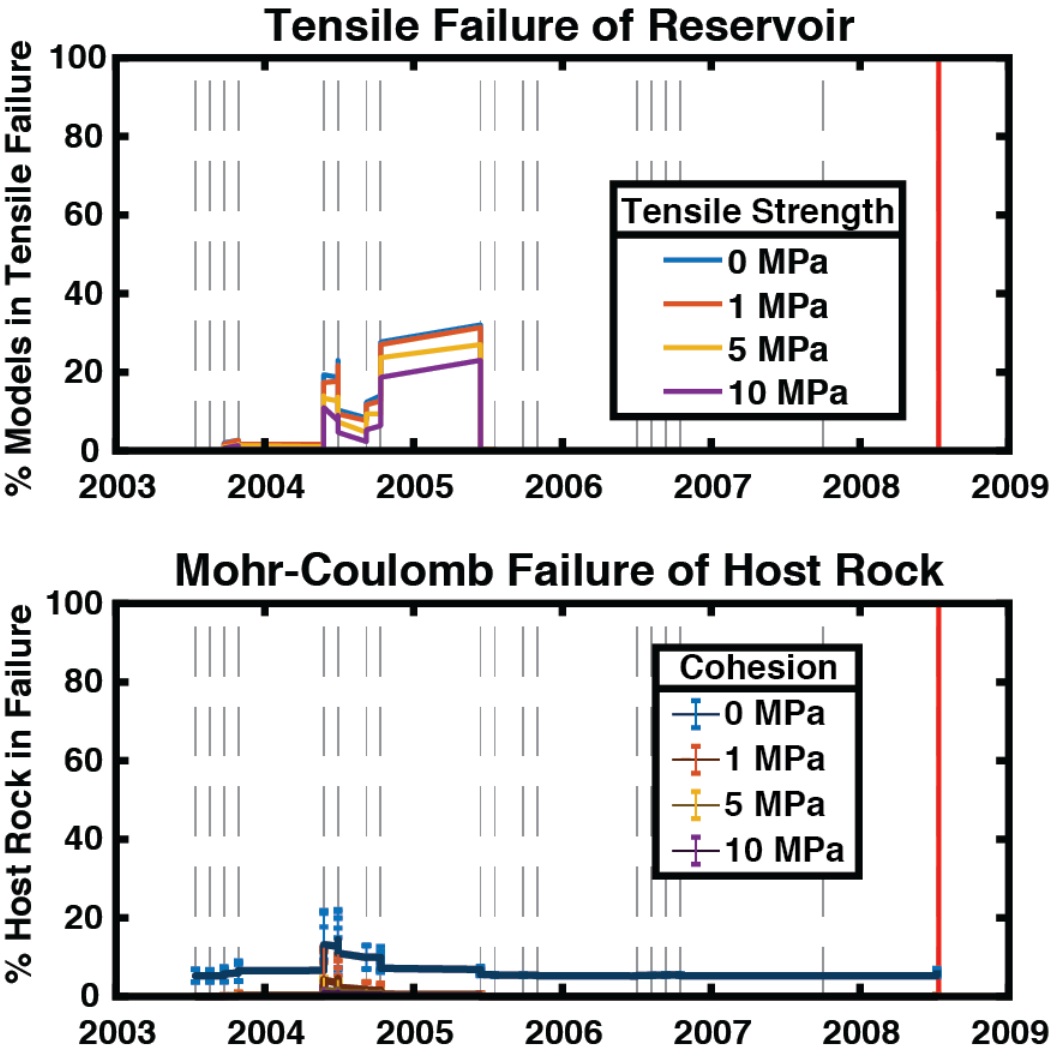

Figure S14. Predicted rates of tensile (top) and Mohr-Coulomb failure (bottom) for the InSAR-only assimilation.

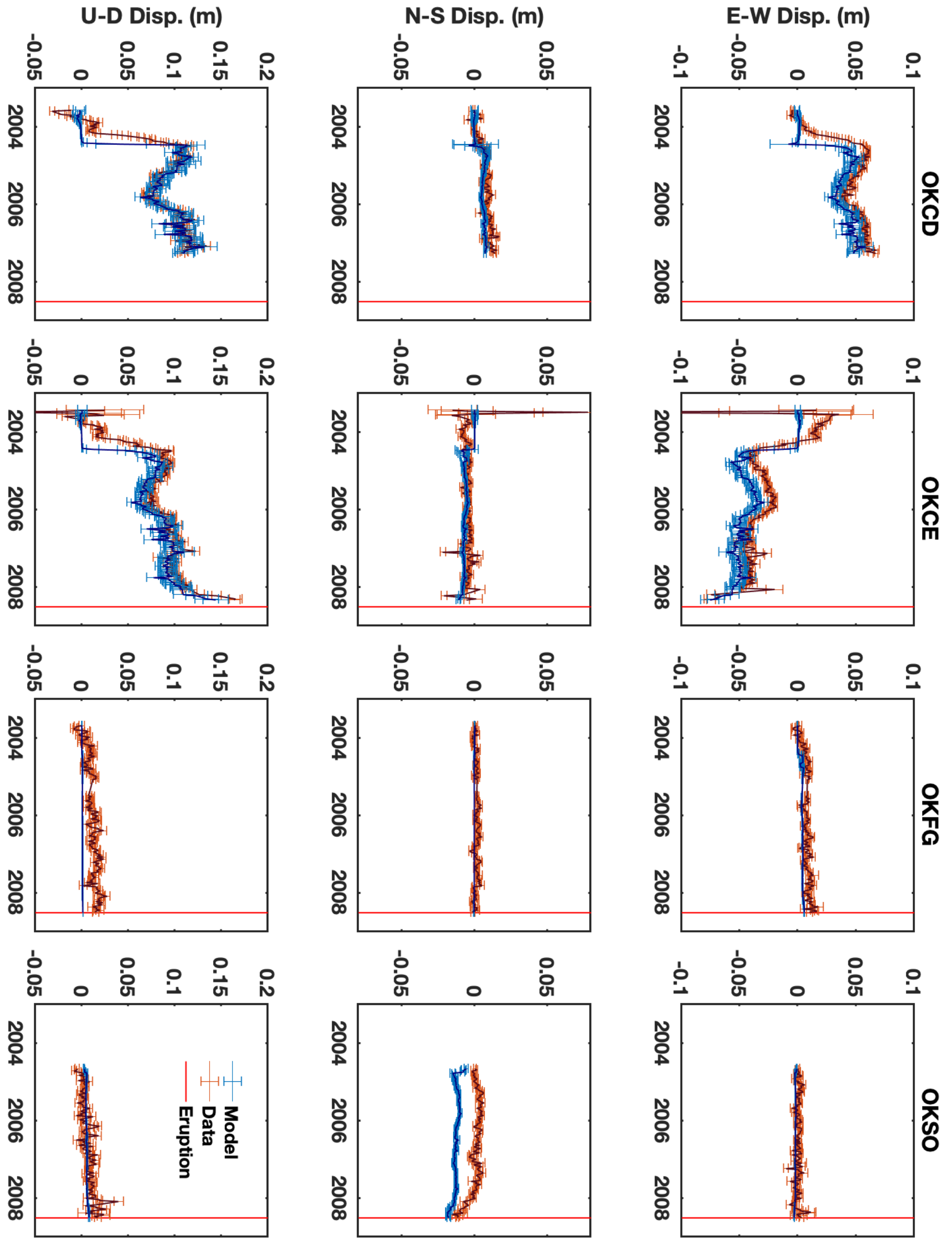

Figure S15. GPS Fit for continuous instruments the joint assimilation with lowered Young's Modulus showing all four continuous sites that were used.

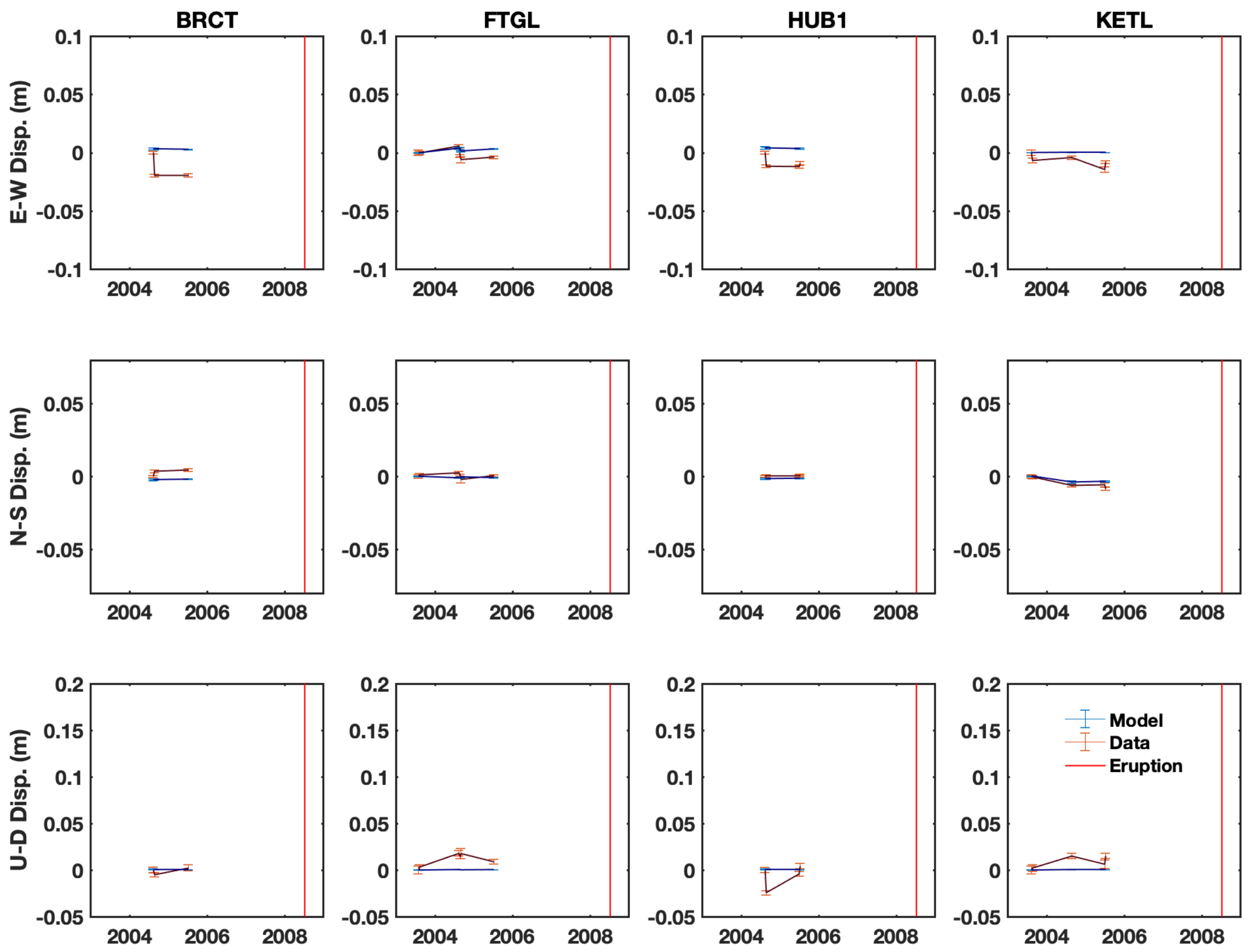
BRCT
FTGL
HUB1
KETL
E-W Disp. (m)
N-S Disp. (m)
U-D Disp. (m)
0.1
0.05
0
-0.05
-0.1
0.2
0.15
2004
2006
2008
Model
Data
Eruption

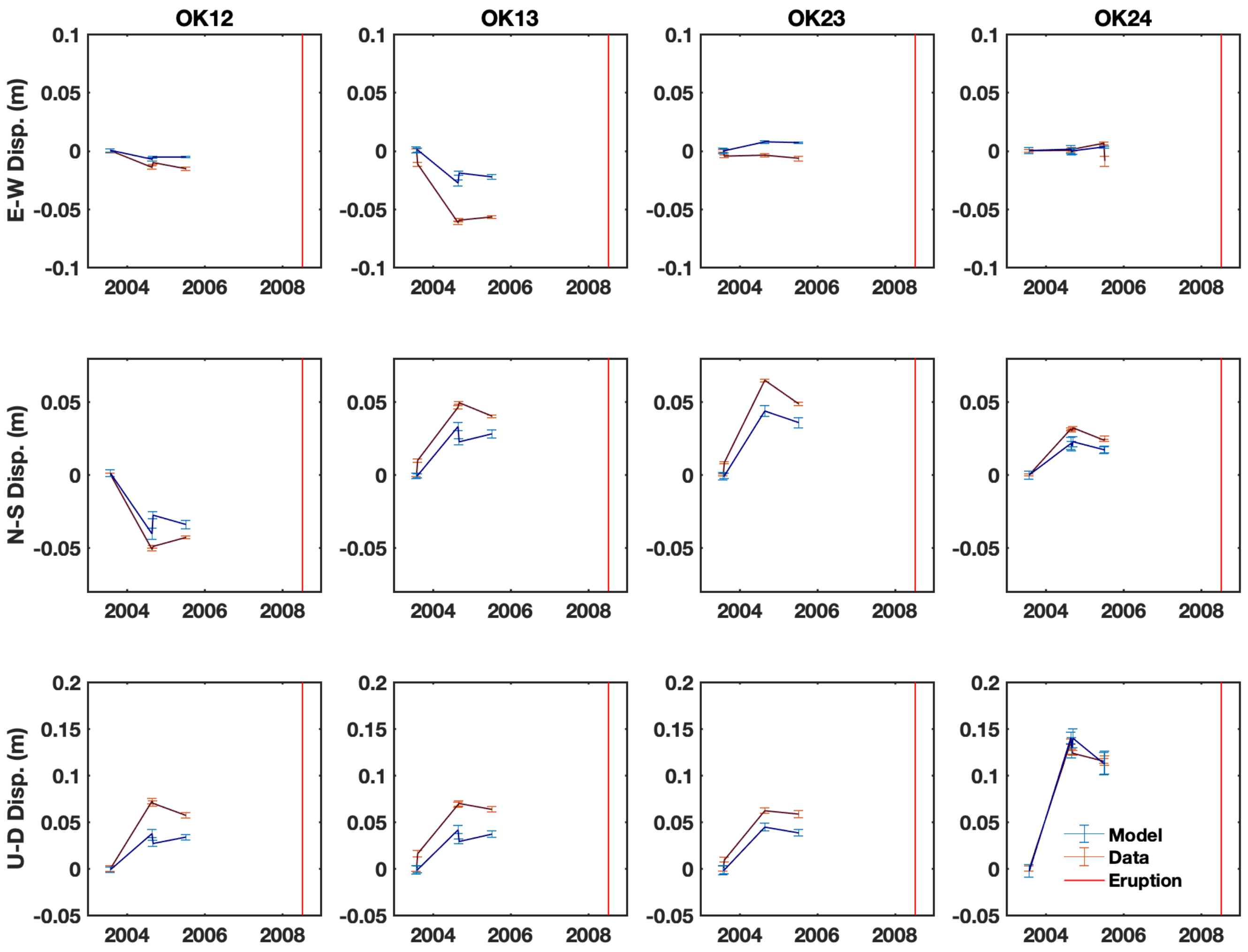
OK12
OK13
OK23
OK24
E-W Disp. (m)
N-S Disp. (m)
U-D Disp. (m)
0.1
0.05
0
-0.05
-0.1
0.2
0.15
2004
2006
2008
Model
Data
Eruption

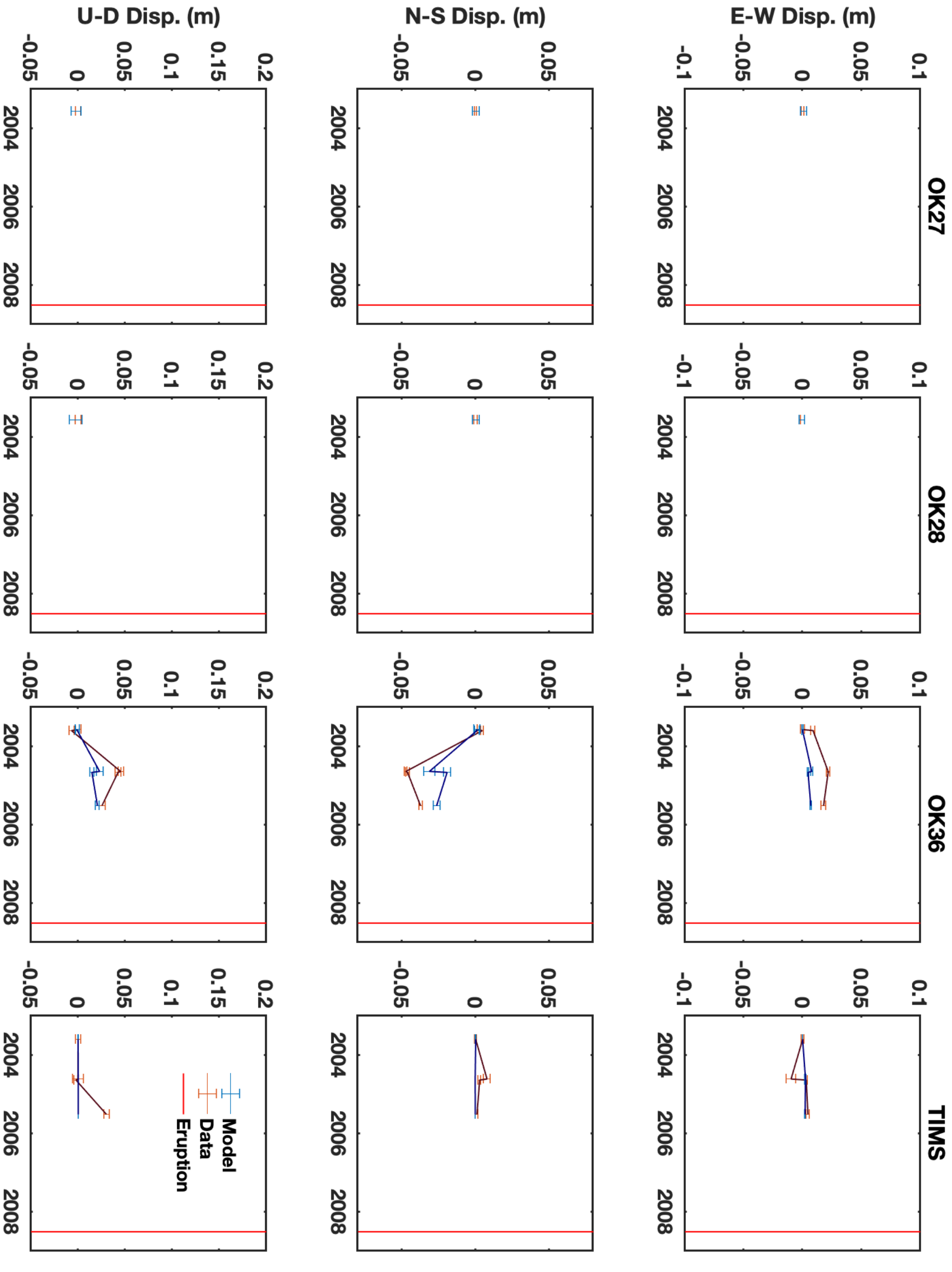

Figure S16. (3 pages) GPS Fit for campaign sites in the joint assimilation with lowered Young's Modulus showing all sites that were used.

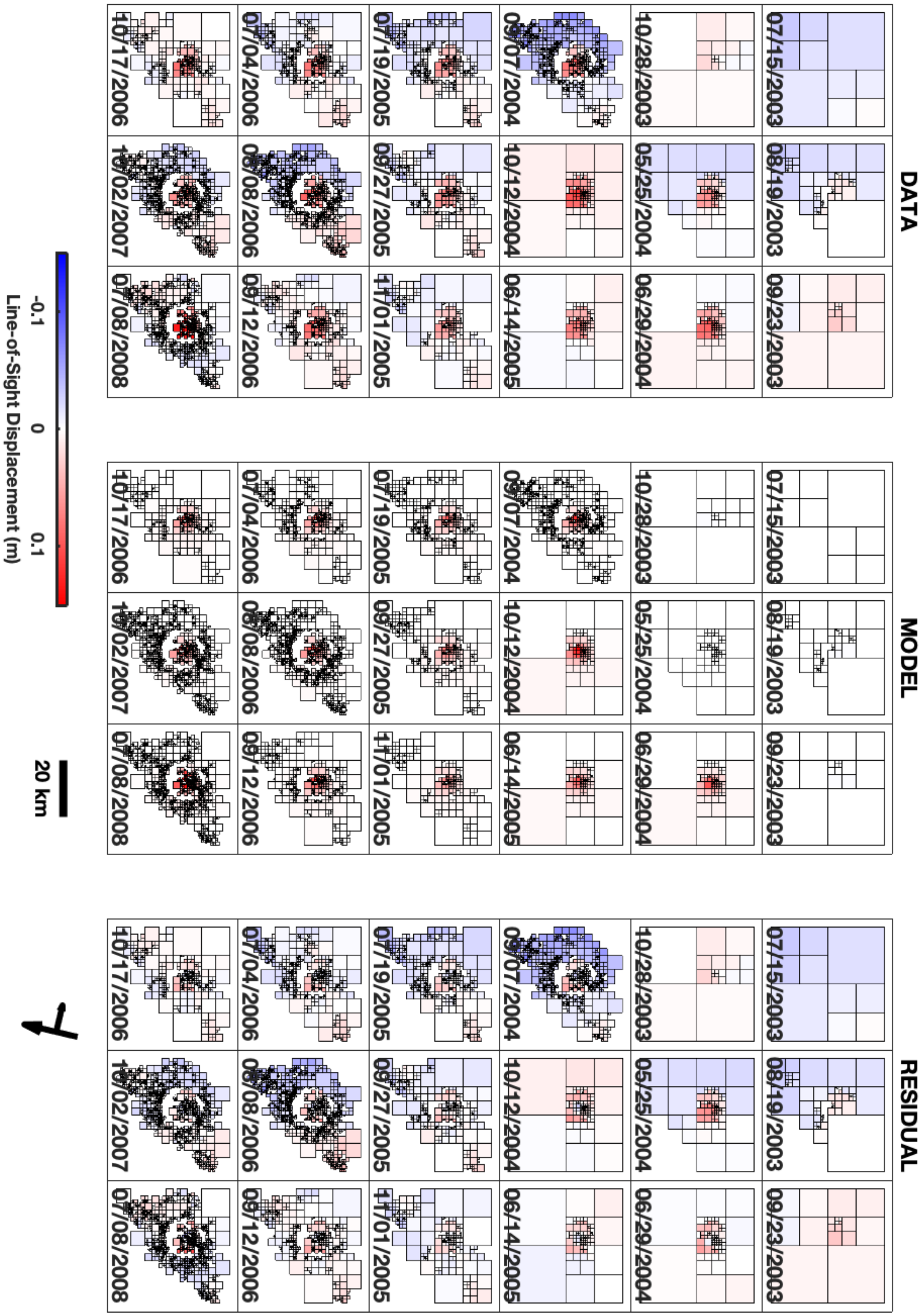

Figure S17. InSAR fit for every InSAR image used in the joint assimilation with lowered Young's Modulus. Cumulative deformation from initial SAR image on 06/10/2003

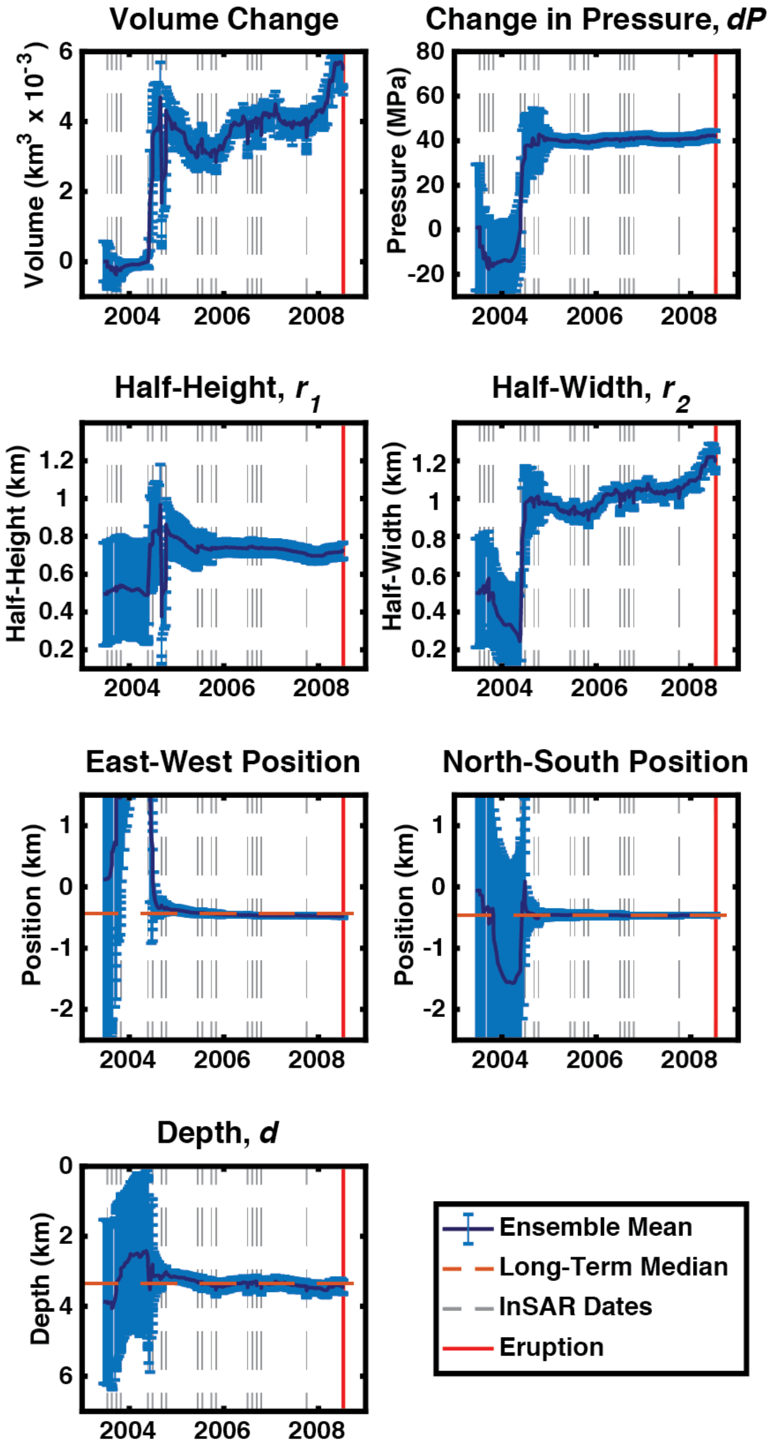

Figure S18. EnKF predictions of model variables for the joint assimilation with lowered Young's Modulus. Uncertainty given by twice the observed standard deviation in each parameter (N = 300)

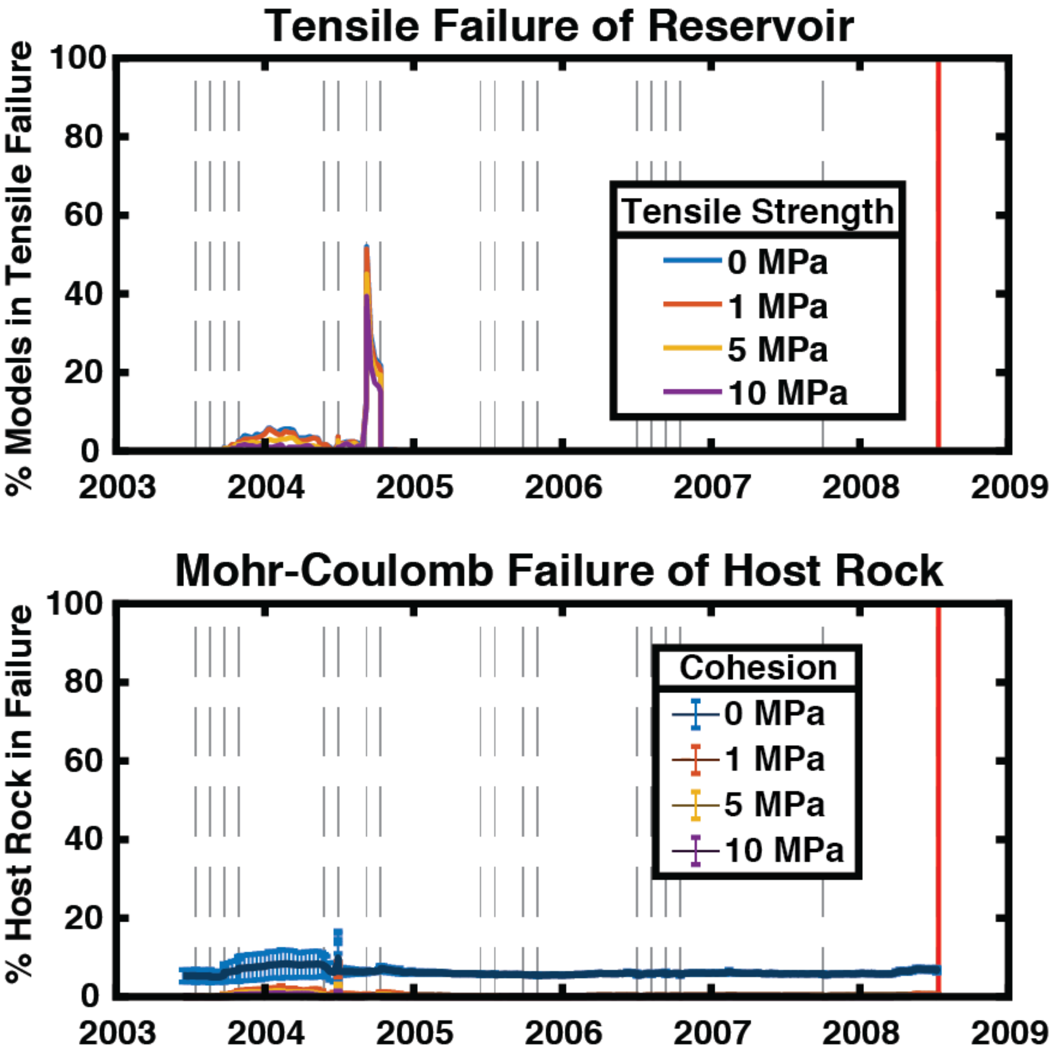

Figure S19. Predicted rates of tensile (top) and Mohr-Coulomb failure (bottom) for the joint assimilation with lowered Young's Modulus.

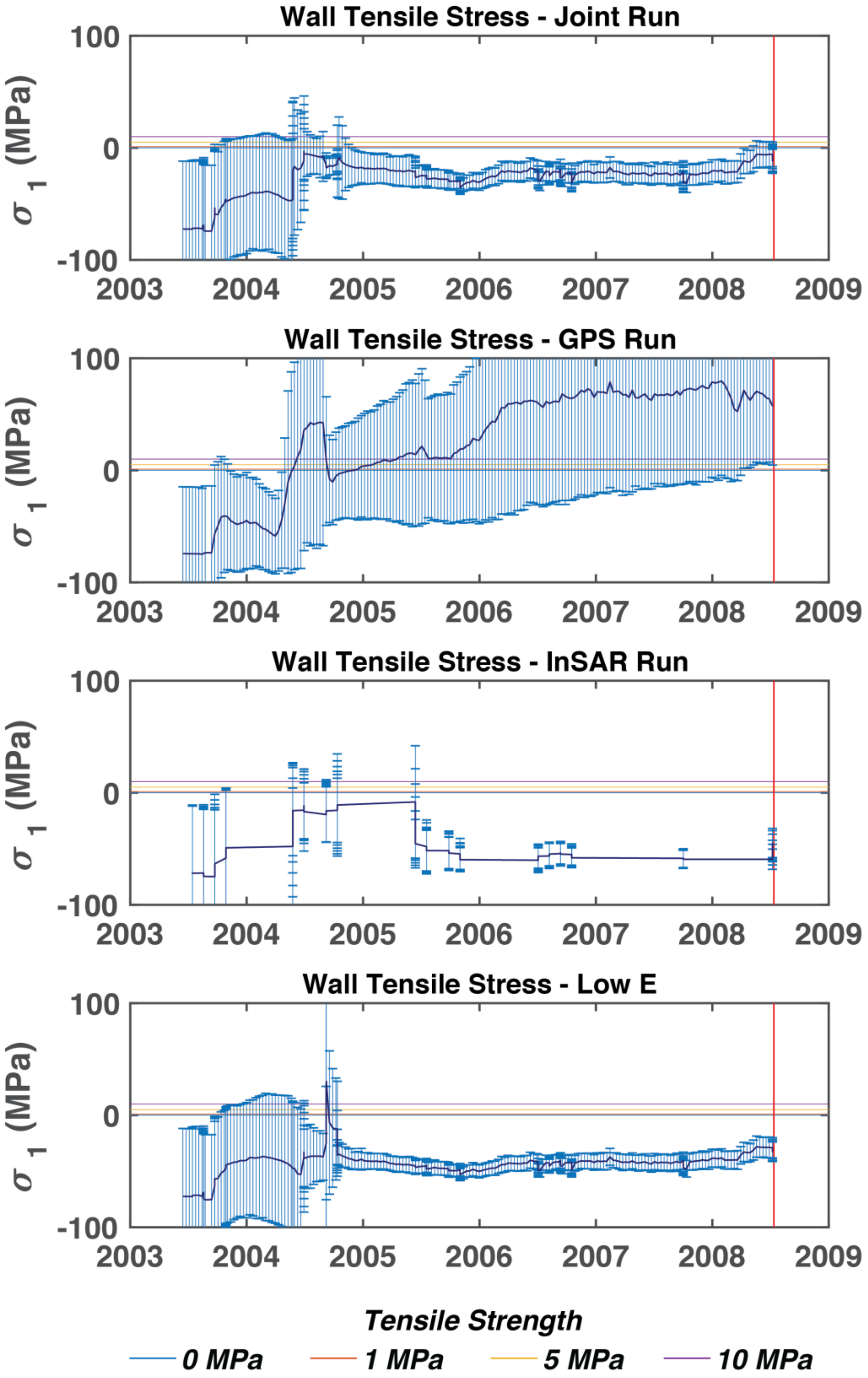

Figure S20. Maximum tensile stress calculated along the reservoir wall by EnKF assimilation at each time step for each assimilation. Solid line indicates ensemble mean with 2σ error bars. Horizontal lines indicate threshold tensile strengths.

Parameter	Description	Value
E	Young's Modulus, GPa	75, 50
g	Gravitational acceleration, m s^{-2}	9.81
N	Number of ensemble members	300
υ	Poisson's ratio	0.25
ρ_r	Host rock density, kg m^{-3}	2500
φ	Angle of internal friction, °	25

Table S1. Model parameters.

Variable	Description
A^a	EnKF analysis ensemble
A	EnKF forecast ensemble
C	Cohesion, Pa
d	Depth to reservoir center, m
D	EnKF measurement matrix
dP	Pressure change, Pa
dV	Volume change, km^3
dX	East-west distance from 168.13° W, m
dY	North-south distance from 53.432° N, m
ε	Strain
G	Shear modulus, Pa
H	vEnKF model operator matrix
K	Bulk modulus, Pa
P	Reservoir wall load, Pa
P_e	EnKF ensemble covariance matrix
r	Horizontal distance, cylindrical coordinate system, m
r_1	Reservoir half-height, m
r_2	Reservoir half-width, m
R_e	EnKF measurement covariance matrix
σ	Stress, Pa
σ_n	Normal stress, Pa
σ_T	Tensile strength of host rock, Pa
θ	Azimuth, cylindrical coordinate system
t	Time
τ	Shear stress, Pa
u_r	Horizontal displacement, m
u_z	Vertical displacement, m
z	Depth, positive up, m

Table S2. Model variables.

Dataset	**Runtime, Hours**
Joint GPS + InSAR	38.0
GPS Only	23.2
InSAR Only	13.8
Low E - Joint	37.7

Table S3. Assimilation runtimes.

Dataset	Variable	Value
Joint GPS + InSAR	r_1, m	743 ± 43.2
	r_2, m	1194 ± 67.0
	d, m	3414 ± 193.2
	dP, MPa	61 ± 3.5
	dX, m	-472± 28.8
	dY, m	-423 ± 24.2
	dV, km^3	0.0054 ± 0.00073
GPS-only	r_1, m	370 ± 102.6
	r_2, m	1553 ± 88.0
	d, m	3100 ± 184.6
	dP, MPa	28 ± 1.6
	dX, m	-576 ± 31.8
	dY, m	-516 ± 30.3
	dV, km^3	0.0021 ± 0.00062
InSAR-only	r_1, m	877 ± 156.9
	r_2, m	1532 ± 60.5
	d, m	3445 ± 188.8
	dP, MPa	28 ± 1.6
	dX, m	80 ± 111.5
	dY, m	-170 ± 96.1
	dV, km^3	0.0048 ± 0.00092
Joint, Low E	r_1, m	724 ± 43.1
	r_2, m	1198 ± 66.5
	d, m	3466 ± 202.0
	dP, MPa	42 ± 2.3
	dX, m	-480 ± 27.4
	dY, m	-463 ± 27.4
	dV, km^3	0.0055 ± 0.00073

Table S4. Mean variable values at final time steps with 2-sigma uncertainties.